Universität Karlsruhe (TH)
Forschungsuniversität • gegründet 1825

IEKP-KA/2008-30

Spektroskopie orbital angeregter (L=1) D_s^{**} Mesonen

Martin Hahn

Diplomarbeit

an der Fakultät für Physik
der Universität Karlsruhe

Referent: Prof. Dr. M. Feindt
Korreferent: Prof. Dr. G. Quast

Institut für Experimentelle Kernphysik

10. Oktober 2008

Deutsche Zusammenfassung

Einleitung und Motivation

Im Quarkmodell exsistieren drei verschiedene Generationen die jeweils aus 2 Quarks bestehen: $\binom{u}{d}, \binom{c}{s}$, und $\binom{t}{b}$. Diese sechs Quarks sind zusammen mit den Leptonen die Grundbausteine der Materie. Neben der Einteilung in verschiedene Generationen zeichnen sich Quarks durch Eigenschaften wie Masse, Ladung, "Geschmacksrichtung", Farbe und Spin aus. Außerdem besitzt jedes Quark einen Antiquarkpartner gleicher Masse und gleichen Spins. Dieser hat entgegengesetze elektrische Ladung sowie entgegengesetze Farbladung. Quarks (q) und ihre Antiteilchen ($\overline{q}$) können nun farblose $q\overline{q}$-systeme, genannt Mesonen, bilden. Da sich die Quarkmassen über mehrere Größenordnungen erstrecken, unterscheidet man zwischen leichten (u,d,s) und schweren (c,b,t) Quarks . Schwer bedeutet in diesem Zusammenhang, dass die Quarkmasse groß ist im Vergleich zur charakteristischen Skala der Quantenchromodynamik (QCD).

Diese Arbeit beschäftigt sich mit der Spektroskopie orbital angeregter (L=1) $c\overline{s}$ Mesonen D_s^{**}. Um die Quantenzahlen sowie die Massen der D_s^{**}-Zustände vorherzusagen, wird die sogenannte effektive Theorie schwerer Quarks (HQET) benutzt. Sie beschreibt die Wechselwirkungen eines Mesonsystems, bestehend aus einem schweren (Q) und einem leichten Quark (q). Im Limit hoher Masse ($m_Q \gg m_q$) kann ein statisches Potential benutzt werden, welches "einengende" (confining), abstoßende und spinabhängige Anteile besitzt.

Für die D_s^{**}-Zustände stehen mehrere theoretische Vorhersagen im Widerspruch zu den experimentellen Ergebnissen. Insbesondere die Massen der D_s^{**}-Zustände $D_{s0}(2317)$ und $D_{s1}(2460)$ werden von den meisten Modellen (vergleiche Tabelle 2.2) rund 100 MeV/c^2 zu hoch vorhergesagt. Außerdem erwartet man nach HQET, dass $D_{s0}(2317)$ und $D_{s1}(2460)$ als breite Resonanzen auftreten. Experimentell misst man jedoch Breiten kleiner 4 MeV/c^2 (vergleiche Tabelle 2.1), was der Vorhersage klar widerspricht. Die D_s^{**}-Spektroskopie bietet die Möglichkeit neue breite Zustände zu entdecken und somit die Diskrepanzen zwischen Theorie und Experiment zu beseitigen. In dieser Arbeit wurden die Zerfallskanäle $D_s^{**} \to D^{*0}K$ und $D_s^{**} \to D^0K$ untersucht. Die entsprechenden experimentellen Daten wurden durch den CDF-II (Collider Detector Fermilab) Elementarteilchendetektor in den Vereinigten Staaten gesammelt.

Benutzte Daten und CDF-II Detektor

Der CDF-II Detektor ist ein Teil des Fermilabs, des größten Technologiezentrums für Hochenergiephysik in den Vereinigten Staaten. Im Teilchenbeschleuniger Tevat-

ron werden Protonen und Antiprotonen auf eine Schwerpunktsenergie von 1,96 TeV beschleunigt um dann im Inneren des CDF-II Detektors zur Kollision gebracht zu werden. Der CDF-II Detektor ist ein symmetrisch um die Strahlachse aufgebauter Universaldetektor. Zur Spurrekonstruktion ist die Strahlachse von verschiedenen Siliziumdetektoren und einer Driftkammer umgeben. Ein Magnetfeld von 1.4 Tesla lenkt geladene Teilchen auf gekrümmte Bahnen ab. Dadurch ist eine Messung des Impulses sowie der Spur der Teilchen möglich. Zur Energiemessung ist der CDF-II Detektor mit einer Reihe von Kalorimetern ausgestattet, die sich außerhalb des Magnetfelds befinden. Der äußerste Teil des Detektors dient zum Nachweis von Myonen, die nur sehr wenig mit dem Detektormaterial wechselwirken und deshalb erst in den Myonkammern detektiert werden.

Aufgrund der hohen Wechselwirkungsrate bei CDF-II können nicht alle gemessenen Ereignisse aufgezeichnet werden. Dies wäre auch wenig sinnvoll da nur wenige Ereignisse von physikalischem Interesse sind. Der "Zweispurtrigger", der für eine Selektion langlebiger Teilchen ausgelegt ist, wählt aus, welche Ereignisse gespeichert werden. Die für diese Arbeit relevanten Daten wurden im Zeitraum Februar 2002 bis Januar 2007 gesammelt. Dies entspricht einer integrierten Luminosität von 1,6 fb^{-1}.

Analyse und Ergebnisse

Um eine Suche nach potentiellen breiten Zuständen in einem möglichst großen Massenbereich im D^0K Spektrum zu ermöglichen, wurden neue Analyseverfahren angewendet. Dazu gehört der sPlot Formalismus, der es ermöglicht NeuroBayes Trainings durchzuführen, die ohne Monte Carlo Modelle auskommen. Unter Verwendung der gut sichtbaren Zustände $D_{s1}(2536)$ und $D_{s2}(2573)$ als untergrundsubtrahierte Signale konnten in einem großen Massenbereich signalartige von untergrundartigen Ereignissen getrennt werden.

Um die Zerfallskette $D_s^{**} \to D^0K \to (K\pi)\,K$ zu rekonstruieren, beginnt man mit der Rekonstruktion des D^0-Zustands. In einem Vertexfit werden zwei beliebige Spuren kombiniert und auf einen gemeinsamen Zerfallspunkt hin überprüft. Zusätzlich wird die rekonstruierte Masse berechnet und auf Konsistenz mit der wirklichen D^0-Masse geprüft. Die so gewonnenen D^0-Kandidaten werden mit den restlichen Spuren kombiniert, um potentielle D_s^{**}-Ereignisse zu erhalten.

Zwei breite Zustände, $D_{sJ}(2860)$, nachgewiesen von BaBar [1], und $D_{sJ}(2700)$, entdeckt durch BaBar und Belle [1, 2] konnten in den hier verwendeten Daten nachgewiesen werden. Es handelt sich um die beiden breiten Resonanzen bei $Q = 0.34$ GeV/c^2 ($D_{sJ}(2700)$) und $Q = 0.5$ GeV/c^2 ($D_{sJ}(2860)$) in Abbildung 0.1.

Zwei weitere Messungen wurden für den Zustand $D_{s1}(2536)$ durchgeführt. Das $D_{s1}(2536)$ zerfällt in $D^{*0}K$, wobei das D^{*0} entweder über ein Photon oder ein neutrales Pion weiterzerfällt:

$$\begin{aligned} D_{s1}(2536) \to D^{*0}K^+ \to \quad & D^0\pi^0K^+ \to \quad K\pi\pi^0K^+ \\ \ldots \to \quad & D^0\gamma K^+ \to \quad K\pi\gamma K^+ \end{aligned} \tag{0.1}$$

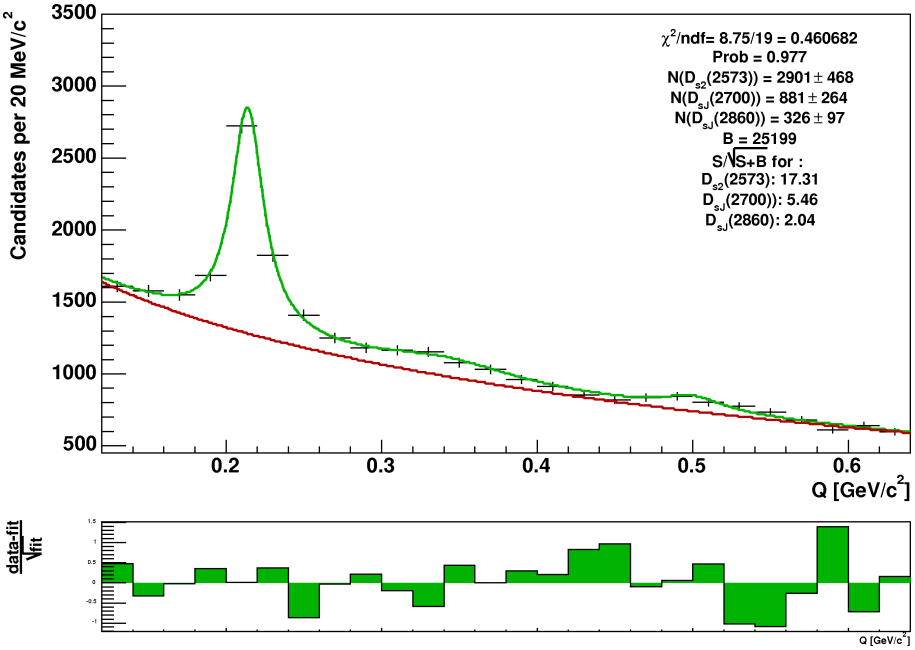

Abbildung 0.1: $D_{s2}(2573)$ zusammen mit $D_{sJ}(2700)$ und $D_{sJ}(2860)$. Q ist definiert als $Q = m_{re}\left(D^0K\right) - m_{re}\left(D^0\right) - m_{pdg}\left(K\right)$, wobei m_{re} rekonstruierte Massen bezeichnet und m_{pdg} für Weltmittelwerte steht [3].

Da der CDF-II Detektor nicht zum Nachweis niederenergetischer neutraler Teilchen entworfen wurde, ist das $D_{s1}(2536)$ im D^0K Spektrum als Reflexion sichtbar. Nun wird die Form der $D_{s1}(2536)-$Resonanz durch das Zerfallsverhältnis $\Gamma_{\pi^0\gamma} = \Gamma(D^*(2007)^0 \to D^0\pi^0)/\Gamma(D^*(2007)^0 \to D^0\gamma)$ sowie durch die Winkelverteilungen des Zerfalls beeinflusst. Zerfällt das D^{*0} über ein neutrales Pion, ist die Resonanz gaußförmig und relativ schmal, wohingegen eine breite plateauförmige Resonanz zu sehen ist, wenn ein Photon beim Zerfall von D_{s1} beteiligt war (vergleiche Abbildung 0.2). Dieses Phänomen kann folglich dazu dienen, $\Gamma_{\pi^0\gamma}$ zu messen. Zusätzlich kann auch das Helizitätsverhältnis $R_\Lambda = |A_{10}|^2 / |A_{00}|^2$bestimmt werden, da die Form der Massenverteilung des $D_{s1}(2536)$ von ihm abhängt. Zur Messung des Verhälnisses von D- und S-Welle $|D/S|$ ist eine zusätzliche Messung der Phase ϕ_{10} zwischen den beiden Helizitätsamplituden notwendig. Die für die Zerfälle in Gleichung 0.1 relevanten Winkelverteilungen sind allerdings unabhängig von ϕ_{10} für unpolarisiertes $D_{s1}(2536)$. Dies macht eine Messung von ϕ_{10} durch die hier verwendeten Daten unmöglich. Folgende Ergebnisse wurden gemessen:

$$\begin{aligned} R_\Lambda &= 2.65 \pm 0.24 \\ \Gamma_{\pi^0\gamma} &= 1.57 \pm 0.06 \end{aligned}$$

Eine Messung von Belle ergab einen Wert von $R_\Lambda = 3.6 \pm 0.3(stat) \pm 0.1(syst.)$[4]. Das Verzweigungsverhältnis $\Gamma_{\pi^0\gamma}$ wurde von BaBar gemessen und beträgt: ($\Gamma_{\pi^0\gamma} = 1.74 \pm 0.02(stat.) \pm 0.13(syst.)$)[5]. Beide Ergebnisse sind konsistent mit den Messungen von Belle und BaBar, da zu den statistischen Unsicherheiten noch systematische Unsicherheiten hinzukommen, die im Rahmen dieser Arbeit nicht bestimmt wurden.

Des Weiteren konnte das $D_{s2}(2573)$ im Zerfallskanal $D_{s2}(2573) \to D^{*0}K$ entdeckt werden, was die weltweit erste Beobachtung des $D_{s2}(2573)$ in diesem Zerfallskanal darstellt (siehe Abbildung 0.2).

Die hier präsentierten Ergebnisse müssen noch durch eine Studie der systematischen Unsicherheiten ergänzt werden. Darüber hinaus sind weitere Messungen vorstellbar: das Produktionsverhältnis für $D_{s1}(2536)$ und $D_{s2}(2573)$ sowie das Verzweigungsverhältnis $D_{s2}(2573) \to D^{*0}K / D_{s2}(2573) \to D^0K$ können aus den vorhandenen Daten bestimmt werden.

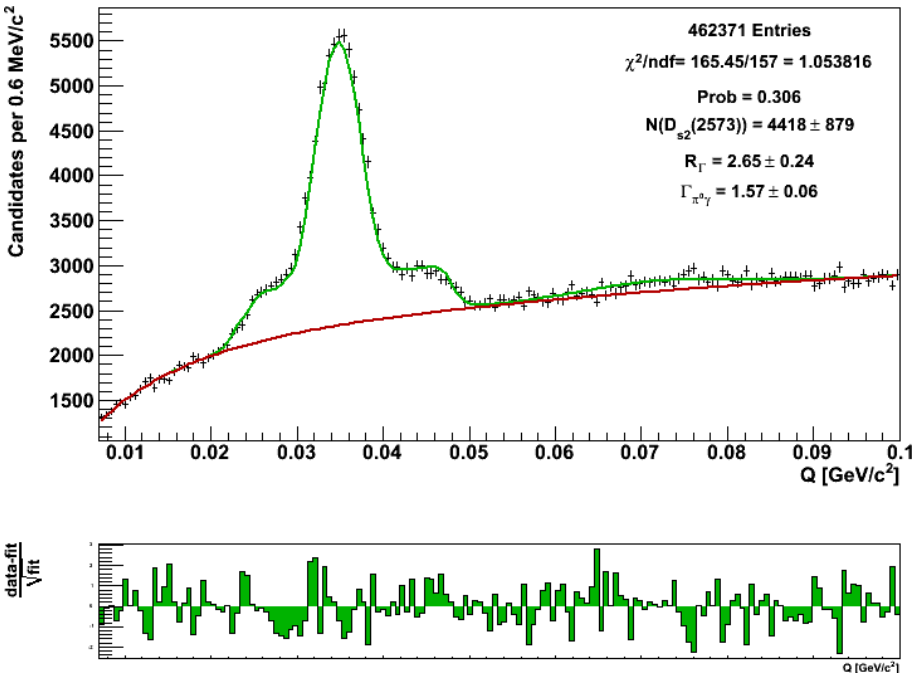

Abbildung 0.2: Messung des Verzweigungsverhältnisses $\Gamma_{\pi^0\gamma}$ und des Amplitudenverhältnisses R_Λ.
Bei $Q = 0.072$ GeV/c^2 ist der Zerfall $D_{s2}(2573) \to D^{*0}K^+$ zu sehen. Die Form des ausgeprägten $D_{s1}(2536)$ Signals wurde benutzt um $\Gamma_{\pi^0\gamma}$ und R_Λ zu messen.

Contents

List of Figures

List of Tables

1 Introduction

The quark model consists of three different generations, each populated by two quarks: $\binom{u}{d}$, $\binom{c}{s}$, and $\binom{t}{b}$. Besides the arrangement in different generations quarks are further classified by numerous degrees of freedom including mass, charge, flavor, color and spin. They can be combined to colorless $q\overline{q}$-doublets and triplets which are called mesons and baryons, respectively. Since quark masses differ over several orders of magnitude quarks are classified in two groups: light (u,d,s) and heavy quarks (c,b,t). In this context heavy means that the quark mass is very large compared to the quantum chromodynamic scale Λ_{QCD}. A meson consisting of one heavy quark (antiquark) and one light antiquark (quark) is referred to as heavy-light quark system.

The states relevant for this thesis are the four orbitally excited (L=1) $c\overline{s}$ mesons (D_s^{**}). To predict their quantum numbers and masses Heavy Quark Effective Theory (HQET) is used. It describes interactions between constituents of heavy-light quark systems. In the limit of very large heavy quark mass a static potential is assumed for the heavy quark. Then the heavy-light system behaves similar to a hydrogen atom where the interaction potential includes confining, Coulomb and spin-dependent components.

In the past, several theoretical models based on HQET made predictions for physical observables which were compared to experimental results in order to determine the validity of these models. In the relatively new D_s^{**} sector these predictions are not consistent with experimental results which is the main motivation to analyze the decay modes $D_s^{**} \to D^0 K$ and $D_s^{**} \to D^{*0} K$ at the Collider Detector at Fermilab (CDF).

Analyzing the ratio of helicity amplitudes $R_\Lambda = |A_{10}|^2 / |A_{00}|^2$ in the decay $D_{s1}(2536) \to D^{*0} K$ is one objective to achieve. The HQET hypothesis of a pure D-wave amplitude for this decay is questionable. It will be shown that the decay $D_{s1}(2536) \to D^{*0} K$ is not compatible with this assumption.

Furthermore the decay $D_{s1}(2536) \to D^{*0} K$ enables the measurement of the branching ratio $\Gamma(D^*(2007)^0 \to D^0\pi^0)/\Gamma(D^*(2007)^0 \to D^0\gamma)$. This is remarkable since the CDF detector was not designed to detect low energetic neutral particles. The proposed method works completely without reconstruction of photons or neutral pions.

Just as important as above objectives is the search for broad resonant D_s^{**} states. $D_{sJ}(2860)$, for example, only seen by the BaBar collaboration[1], has not been confirmed by Belle[2]. In this thesis, the two states $D_{sJ}(2860)$ and $D_{sJ}(2700)$ are seen at CDF, in addition, the $D_{s2}(2573)$ is seen.

To achieve these goals a new statistical technique, the so called "sPlot formalism" is used to prepare the data for NeuroBayes, a sophisticated neuronal network package. NeuroBayes was enhanced in order to make a training with sPlot weights possible.

It will be shown that Neural Networks trained on known physical states at a given

mass can be applied to a wide mass window for discriminating between resonances and combinatorial background. This technique can be exploited for searching new resonances or rare decays.

2 Comparison of Experimental Results and Theoretical Expectations for D_s^{**}

2.1 Heavy Quark Effective Theory (HQET)

The two-quark states D_s^{**} are composed of a charm and a anti-strange quark: $c\bar{s}$. Because the charm quark is much heavier than the strange quark one speaks of a heavy-light quark system. In general, systems containing heavy quarks are easier to understand than those consisting of light quarks. One reason is asymptotic freedom. As quarks approach each other the strong interaction coupling constant α_s becomes small. In that domain strong interactions can be calculated pertubatively and are much like electromagnetic interactions. With larger distances the coupling gets stronger and nonperturbative phenomena do not allow an easy description of the interactions between the quarks. It turns out that the typical size of hadrons, $R_h = 1$ fm, is the characteristic distance which approximately separates the areas of small and large coupling. Related to that distance is the energy scale $\Lambda_{QCD} \approx 0.2$ GeV. Now one speaks of heavy quarks if the mass of the quark is much bigger than the QCD scale:

$$m_Q \gg \Lambda_{QCD} \Leftrightarrow \lambda_Q \sim \frac{1}{m_Q} \ll R_h \sim \frac{1}{\Lambda_{QCD}} \sim 1 \text{ fm} .$$

where λ_Q is the Compton wavelength of the heavy quark Q.

As a first approach one basically considers the limit of infinite heavy quark mass. In that limit, the dynamics of the heavy-light quark system $Q\overline{q}$ is independent of mass and spin of the heavy quark. Thus one can use the total angular momentum of the light quark j_q as a good quantum number and couple it to the spin of the heavy quark s_Q.

$$\begin{aligned} \vec{J} &= \vec{j_q} + \vec{s_Q} \\ \vec{j_q} &= \vec{s_q} + \vec{L} \end{aligned}$$

where $\vec{j_q}$ is calculated by adding the spin of the light quark $\vec{s_q}$ and the orbital angular momentum $\vec{L}$. Consequently for every value j_q a doublet of degenerated states is obtained.

In reality quarks have finite mass. Therefore relativistic effects can no longer be neglected. Spin symmetry is broken and the doublet states split. The corresponding corrections are of order $\frac{1}{m_Q}$.

For the orbitally excited D_s^{**} HQET predicts four different possible states with $L = 1$. Hence the total angular momentum of the light quark can take the values

HQET	$D_{s0}(2317)$	$D_{s1}(2460)$	$D_{s1}(2536)$	$D_{s2}(2573)$
J^P	0^+	1^+	1^+	2^+
j_q^P	$\frac{1}{2}^+$	$\frac{1}{2}^+$	$\frac{3}{2}^+$	$\frac{3}{2}^+$
wave	s	s	d	d
Γ_{HQET}	broad	broad	narrow	narrow
Γ_{exp}	<3.8 MeV , CL=95% [6]	<3.5 MeV , CL=95% [6]	<2.3 MeV , CL=90% [7]	20 ± 5 MeV , (PDG average)

Table 2.1: D_s^{**} states as expected in HQET and their measured width Γ_{exp}.

$D_{s0}(2317)$	$D_{s1}(2460)$	$D_{s1}(2536)$	$D_{s2}(2573)$	ref
2480	2550	2550	2590	[8, Godfrey]
2380	2510	2520	2520	[9, Zeng]
2388	2521	2536	2573	[10, Gupta]
2508	2569	2515	2560	[11, Ebert]
2455	2502	2522	2586	[12, Lande]
2487	2605	2535	2581	[13, Di Pierro]
2339	2496	2487	2540	[14, Matsuki]
2329	2474	2526	2577	[15, Close]
2317.8±0.6	2459.6±0.6	2535.35±0.34±0.5	2572.6±0.9	PDG

Table 2.2: D_s^{**} masses in MeV: Theory and experiment

$j_q = \{\frac{1}{2}, \frac{3}{2}\}$. Combining j_q and the spin of the heavy quark results in $J = \{0, 1, 1, 2\}$. Table 2.1 fixes the notation and summarizes the properties of the four D_s^{**} states.

2.2 Motivation and Goals

In the D_s^{**} sector some measurements contradict the theoretical predictions.

First one has to point out that in HQET the $j_q = \frac{1}{2}$ doublet states are expected to be broad resonances. But the experimentally found $D_{s0}(2317)$ and $D_{s1}(2460)$ states are not even approximately broad(see table 2.1).

Second the calculated masses do not agree with experimental results. Table 2.2 summarizes theoretical expectations and the measured masses. $D_{s0}(2317)$ lies approximately 160 MeV below the majority of model computations. Also for the second state in the $j_q = \frac{1}{2}$ multiplet, the $D_{s1}(2460)$, the measured values lie always too low in the D_s^{**} spectrum. Only the models of Madsuki [14] and Close [15] are capable of describing the low $D_{s0}(2317)$ and $D_{s1}(2460)$ masses. Madsuki uses a semi-relativistic Hamiltonian which includes Coulomb-like as well as confining scalar potentials. Corrections up to the second order in $1/m_Q$ for the masses and wave functions are calculated. Close assumes that all known D_s states are dominated by simple $c\bar{s}$ content.

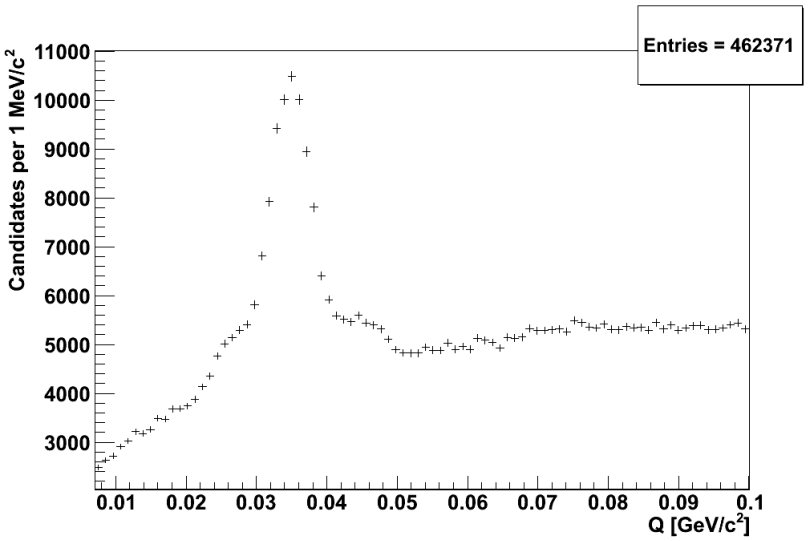

Figure 2.1: $D_{s1}(2536)$ signal events optimized on significance. Q is defined as $Q = m_{re}\left(D_s^{**}\right) - m_{re}\left(D^0\right) - m_{pdg}\left(K\right)$, where m_{re} denotes reconstructed masses and m_{pdg} is the world average given by Particle Data Group[3].

He uses a scalar confining potential and a short range coloumbic vector potential to describe the coupling. His proposed D_s spectrum does also predict the masses of the recently found $D_{sJ}(2860)$ [1] and $D_{sJ}(2700)$ [1, 2]. These newly found resonances can decay to D^0K and can possibly be seen at CDF II. A search for these or even other D_{sJ} states represents one part of this thesis.

Third a paper recently published by Belle [4] has measured the ratio of D- and S-wave amplitudes $|D/S| = 0.63 \pm 0.07 \pm 0.02$ in the decay $D_{s1}(2536) \rightarrow D^*K_s^0$ what clearly contradicts the HQET prediction of a pure d-wave decay. The measured amplitudes even tell us that the S-wave dominates in the decay.

The strong deviations from expectations point to a lack of understanding in the heavy light meson sector and leave much room for exotic models. For example one could imagine DK molecules [16], Tetra quarks [17, 18, 19] or Coupled channel models [20, 21]. The latter assumes that $D_{s0}(2317)$ and $D_{s1}(2460)$ are mostly $c\overline{s}$ states which are heavily renormalised by mixing with the DK and DK^* continua [22]. This approach requires the weakest extension of the quark model [23].

Another objective of this thesis is the measurement of the D- and S-wave amplitudes mentioned above in the $D^{*0}K$ mode. Since D^{*0} decays in $D^0\pi^0$ or $D^0\gamma$, this measurement does not seem possible because low energetic neutral particles can not be reconstructed at CDF-II. This implies that an angular analysis is not feasible due to the missing helicity angle of the D^{*0}. However, the mass line shape of $D_{s1}(2536) \rightarrow D^{*0}K$ turned out to be dependent on the angular distributions. This relationship will be exploited to extract qualitative information about the amplitudes. To explain the mass line shape of $D_{s1}(2536)$ shown in Figure 2.1 one has to know the

two possible decay chains for $D_{s1}(2536)$.

$$\begin{aligned} D_{s1}(2536) \to D^{*0}K^+ \to \quad & D^0\pi^0K^+ \to \quad K\pi\pi^0K^+ \\ \ldots \to \quad & D^0\gamma K^+ \to \quad K\pi\gamma K^+ \end{aligned}$$

They only differ from each other in the neutral particle which can either be a pion or a photon. In case of a pion π^0 its momentum in the rest frame of D^{*0} is small in comparison to the photon's momentum in the same rest frame. This implies that also D^0 carries less momentum if the decay processes via a pion, hence it is closer to D^{*0}'s momentum. So when a pion is created the peak is narrow and gaussian. In contrast if a photon is present in the decay a broad structure which emerges at both sides of the narrow Gaussian signal is seen.

This effect can be exploited to measure the branching ratio $\Gamma(D^0\pi^0)/\Gamma(D^0\gamma)$ although neither a photon nor a pion have ever been detected. The following list summarizes the objectives covered in this thesis:

1. Search for broad resonant D_s^{**} states, especially $D_{sJ}(2700)$ and $D_{sJ}(2860)$ in the D^0K decay channel. The ansatz followed uses $D_{s1}(2563)$ and $D_{s2}(2573)$ background-subtracted signal events for discriminating between resonances and combinatorial background.

2. It will be shown that the $D_{s1}(2536) \to D^{*0}K$ is not compatible with the assumption of pure D-wave decay.

3. Measurement of the branching ratio
$\Gamma_{\pi^0\gamma} = \Gamma(D^*(2007)^0 \to D^0\pi^0)/\Gamma(D^*(2007)^0 \to D^0\gamma)$

4. Measurement of the ratio of helicity amplitudes R_Λ in the decay $D_{s1}(2536) \to D^{*0}K$

5. Enhancement of the NeuroBayes package in order to make this analysis possible. Neurobayes[24] was adapted to make a correct treatment of sPlot weights possible. These are used by the sPlot[25] method, a statistical tool to unfold data distributions which allows to extract pure signal distributions out of a data sample where background and signal events are mixed together.

3 The CDF Experiment

3.1 Fermilab and Tevatron

The Fermilab accelerator complex is the largest laboratory for high energy physics in the Unites States of America. The two main accelerator rings seen in Figure 3.1 give a good impression of its size.

The Tevatron, four miles in circumference, is one of the world's highest-energy particle accelerator, producing $p\bar{p}$ collisions at the energy of 1.96 TeV. Its 1000 superconducting magnets are cooled by liquid helium to 4.3 K. Its low-temperature cooling system was the largest ever built when it was placed in operation in 1983. Protons and anti-protons circle around the Tevatron at 99.9999 percent of the speed of light in vacuum. Accelerated to such a high velocity they complete the four-mile course nearly 50 thousand times a second. The collision rate is almost two million each second.

The detectors CDF-II and D0 are located at opposite sides in the Tevatron. They record the particles emerging from millions of collisions per second.

Figure 3.1: Aeroshot of the Fermilab: the ring in the foreground is the Main Injector and in the background one can see the Tevatron.

Three major components of the Standard Model were discovered at Fermilab: at first the bottom quark in May-June 1977 and the top quark in February 1995. In July 2000, Fermilab experimenters announced the first direct observation of the tau neutrino, the last fundamental particle to be observed.

3.1.1 The Accelerator Chain

To achieve a beam energy of 980 GeV the protons and anti protons have to pass different stages of acceleration(see Figure 3.2). The chain of acceleration starts with the Cockcroft-Walton where negative hydrogen ions are produced and then transferred to the Linear Accelerator (LINAC). After passing the LINAC all electrons are stripped and a pure proton beam enters the first synchrotron, the so called Booster. Finally in the two main accelerating units, the Main Injector and the Tevatron the beam is accelerated to its final energy of 980 GeV. A more detailed description, especially concerning anti protons is given in the following section.

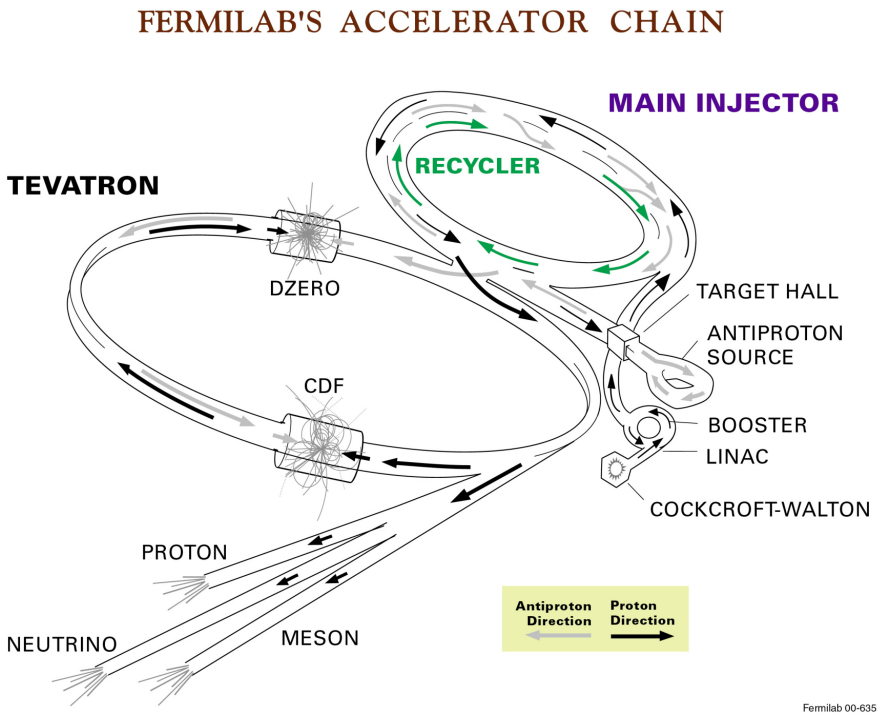

Figure 3.2: The Accelerator Chain.

3.1.2 Cockcroft-Walton

The impressive Cockcroft-Walton voltage multiplier shown in Figure 3.3 provides the first stage of acceleration. Inside this device, negative hydrogen ions are produced.

The resulting negative ions, each consisting of two electrons and one proton, are attracted to a positive voltage and accelerated to an energy of 750 keV. This is about thirty times the energy of the electron beam in a television's picture tube.

Figure 3.3: Picture showing the Cockcroft-Walton preaccelerator used a CDF II.

3.1.3 Linear Accelerator (LINAC)

First the negative hydrogen ions form the Cockcroft-Walton are accelerated in a 201 MHz drift-tube linac(see Figure 3.4), though five large tanks, to 116 MeV.

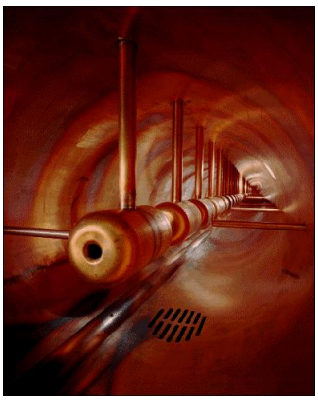

Figure 3.4: Photo from inside of the drift-tube linac, which normally is closed up and under vacuum.

Afterwards the beam is compressed through a 4 m radio frequency transition section to match the 201 MHz beam into the 805 MHz radio frequency structure (rf-structure), and change the transverse focussing. Finally through seven 805 MHz side-coupled

cavity structures shown in Figure 3.5 the hydrogen ions are accelerated to the energy of 401.5 MeV.

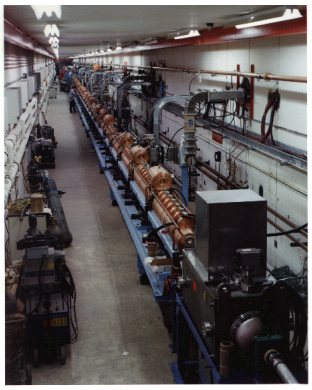

Figure 3.5: 805 MHz Side-coupled Cavity Linac.

3.1.4 The Booster

The 400 MeV line transfers the beam from LINAC to the Booster, bending the beam vertically 4.6 m. But before the beam can enter the Booster the hydrogen ions pass through a carbon foil that strips off the electrons and permits only the protons to pass through.The Booster accelerator is approximately 150 m diameter proton synchrotron with an injection energy of 400 MeV and an extraction energy of 8 GeV. It is considered a "fast cycling" machine, cycling at 15 Hz. A resonant power supply system uses a sinusoidal current waveform to excite the magnets. The Booster is made up of 96 combined function magnets in a series of 24 repeating periods. Their magnetic field varies from about 0.0740 T at injection to 0.7 T at extraction. The Booster tunnel shown in Figure 3.6 is a concrete tunnel 2.4 m high and 3 m wide, covered by 4.6 m of earth shielding.

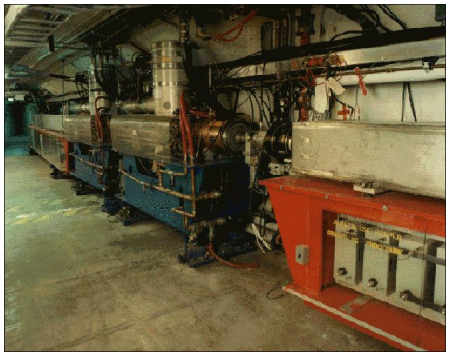

Figure 3.6: Booster synchrotron.

3.1.5 Anti Proton Source

Before the Main Injector and the Tevatron are explained we will briefly discuss why anti protons are used in the experiment and how they are generated.

There is one great advantage of using both, protons and anti protons in one experiment: Since protons and anti protons have opposite electric charge, they will travel in opposite directions through the magnets used in the synchrotron's . So an antiproton-proton collider can be built with one ring of magnets instead of two.

The disadvantage of antiproton-proton collisions is that one has to design and build an anti proton source, a difficult and expensive undertaking. The Anti-Proton Source consists of three major components:

1. The Target Station
2. The Debuncher, an 8 GeV synchrotron
3. The Accumulator, an 8 GeV synchrotron

3.1.5.1 The Target Station

A beam of 120 GeV protons from the Main Injector is smashed on to a Nickel Target every 1.5 s. In the collisions many particles are created. For every 1 million protons that hit the target, only about twenty 8 GeV anti protons survive to make it into the Accumulator.
The anti protons come off the target at many different angles. They are focused into a beam line with a Lithium lens. The beam after the Lithium lens contains many different particles besides anti protons. Many of these particles are filtered away by sending the beam through a pulsed magnet which acts as a charge-mass spectrometer.

3.1.5.2 The Debuncher

The anti protons coming from the Nickel Target will have a wide spread in energy due to scattering and because they were produced over a wide energy range. They will also be bunched because the proton beam is bunched.
The Debauchee rf-cavity will cause the low energy particles to be accelerated and the high energy particles to be decelerated. As this process happens over and over, the energy spread will be reduced.
The debunching process takes about 100 ms. In the rest of the time (the anti protons can stay up to 1.5 s in the Debuncher) stochastic cooling is performed before the beam is transferred to the Accumulator.

3.1.5.3 The Accumulator

The Accumulator can store an anti proton beam over many hours. It accumulates anti protons and brings them to the desired momentum. This is accomplished by stochastic cooling and rf-systems.

3.1.5.4 Stochastic cooling

The anti protons leave the target at a wide range of energies, positions and angles. To remove this randomness stochastic cooling is used in both the Debuncher and the Accumulator. It is essential to get a dense and localized beam of anti protons. Simone van der Meer won the Nobel prize for its invention. Here only a short explanation is given.

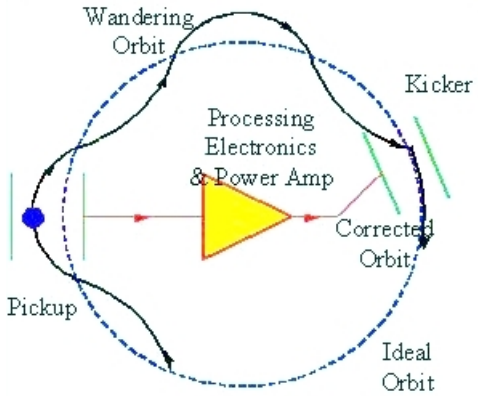

Figure 3.7: The feedback mechanism in Stochastic Cooling.

Stochastic cooling uses feedback. This is illustrated in Figure 3.7. A pickup electrode measures an "error" signal for a given particle. This "error" signal could be that particle's position or energy. Then this "error" signal is processed and amplified. Afterwards the opposite of the "error" signal is applied to the particle at the kicker to bring it in an corrected orbit.
Usually the pickups are cooled to liquid Nitrogen temperatures (77.36 K) or to liquid Helium temperatures (4.22 K) to reduce the effect of thermal noise .

3.1.6 The Main Injector

The Main Injector is the first synchrotron where both, protons and anti protons are accelerated.

- Protons at 8 GeV from the Booster are injected and accelerated to 120 GeV for fixed target operation or 150 GeV for injection into the Tevatron.
- Anti protons at 8 GeV from either the Accumulator or the Recycler are accelerated to 150 GeV in the Main Injector and then injected into the Tevatron.

Figure 3.8: View of the Main Injector tunnel

In Figure 3.8 the Main Injector is the structure at the bottom of the picture. Additionally the Recycler consisting of permanent magnets is installed at the ceiling of the same tunnel. It is used to store anti protons from the Accumulator and the Tevatron respectively.

3.1.7 The Tevatron

In the Tevatron 36 bunches of protons and anti protons cycle around in opposite direction in two separated rings.
After accelerating the beam to its maximum beam energy of 980 GeV is reached the Tevatron enters in the so called "collision mode". For about 20 hours it stays in this mode and collisions are continuously produced.
There are some remarkable features of the Tevatron:

- There are about 1000 superconducting magnets in the Tevatron
- The current flowing through a magnet is more than 4000 Amperes
- The magnets are kept at 4.3 Kelvin, the magnetic field is 4.2 Tesla

- The cryogenic cooling system can deliver 1000 liters per hour of liquid helium at 4.2 K

In Figure 3.9 a photo of the Tevatron tunnel is shown to get an idea of the circumference of this ring accelerator.

Figure 3.9: The Tevatron tunnel

3.2 The CDF II Detector

The following description of the detector components is mainly taken from [26, 27, 28, 29, 30, 31, 32]. We will start with a brief general discussion of CDF II followed by a more elaborated description of the detector components starting with the innermost part, Layer 00. Then we will subsequently describe the next parts till the outermost part of the detector: the Muon Chambers.

The CDF II detector is a multipurpose detector designed to precisely measure the properties of charged particles. Figure 3.10 shows a schematic view of this complex device with all its components.

The detector features fast energy measurements through its calorimetry systems, reliable tracking information through its silicon systems and drift chambers which supplement the muon chambers in providing precise tracking information for muons.

The sectional drawing shown in Figure 3.11 illustrates the dimensions(r,z) and the coverage in pseudorapidity ($\eta = -\ln(\tan(\frac{\theta}{2}))$ with θ the polar angle) for several detector components.

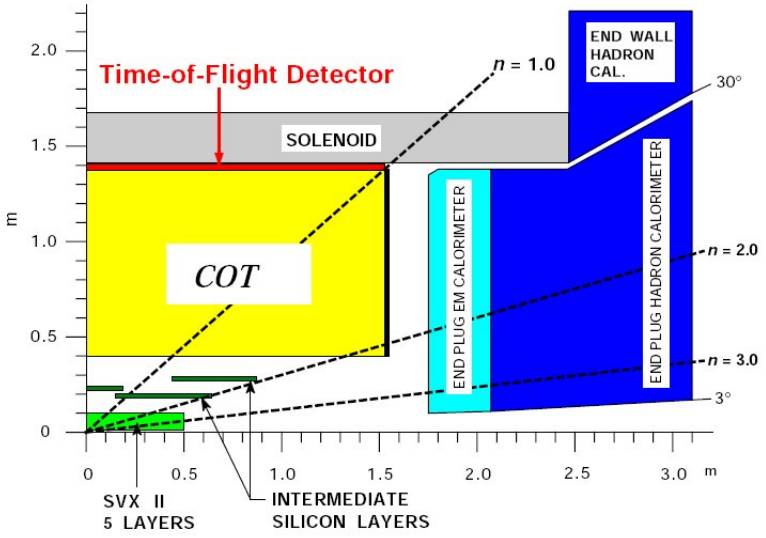

Figure 3.11: A cutaway view of one quadrant of the inner portion of the CDF II detector showing the tracking region surrounded by the solenoid and endcap calorimeters

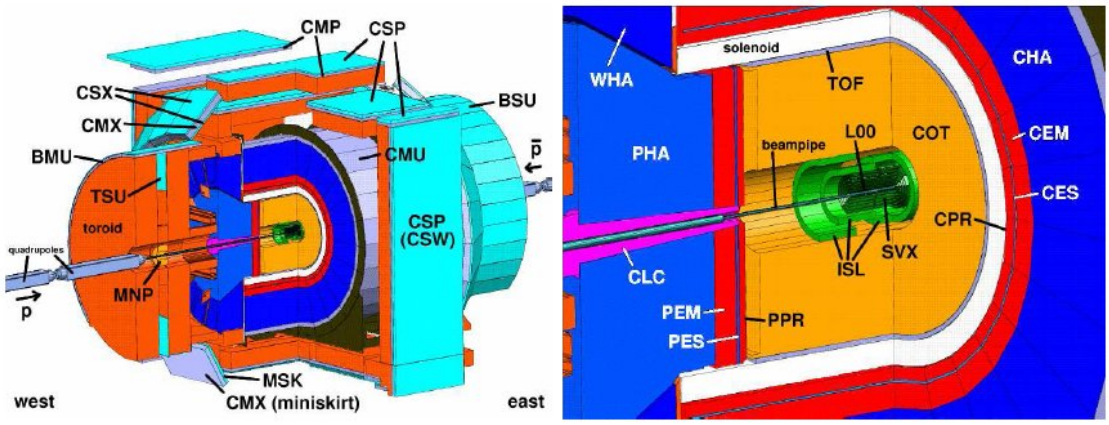

Figure 3.10: Isometric view of the CDF II detector.

List of abbreviations for the left picture:

CMP: Central Muon Upgrade

CSP: Central Scintillator Upgrade

CSX: Central Scintillator Extension

CMX: Central Muon Extension

BMU: Barrel Muon Chambers

TSU: Toroid Scintillator Upgrade

MNP: Miniplug forward Calorimeter

MSK: Miniskirt Muon Scintillator

CMU: Central Muon Chambers

BSU: Barrel Scintillator Upgrade

List of abbreviations for the right picture:

L00: Layer 00

SVX: Silicon Vertex Detectors

ISL: Intermediate Silicon Layers

COT: Central Outer Tracker

TOF: Time Of Flight Detectors

CPR/PPR: Central/end-Plug Preradiator Chambers

CES/PES: Central/end-Plug Electro-Magnetic Shower detectors

CEM/PEM: Central/end-Plug Electro-Magnetic calorimeter

CHA/PHA: Central/end-Plug HAdron calorimeter

WHA: end-Wall HAdron calorimeter

CLC: Cherenkov Luminosity Counters

3.2.1 Silicon Detector

The silicon detector consists of 8 layers of double-sided silicon sensors divided into three subsystems, SVXII and ISL, and L00.

Layer 00

Because it is mounted closest to the beam, Layer 00 consists of single-sided silicon detectors with a guard structure designed to minimize leakage currents. No double-sided silicons are used due to the high radiation at the innermost layer.

Two widths of sensors (8.4 and 14.6 mm) are interleaved in a 12-sided pattern that is physically mounted on and supported by the beam pipe. Layer 00 provides the first ϕ-measurement. In the schematic view of the silicon detector layout in Figure 3.12 Layer 00 is the innermost layer.

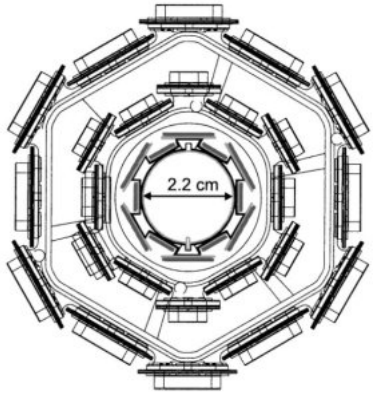

Figure 3.12: Innermost three layers of the CDF Run II silicon system, showing Layer 00 along with the first two layers of the SVX II subsystem.

Silicon Vertex Detectors (SVX-II)

The SVX-II is composed of five layers. In each layer double-sided silicon strip sensors are used to detect hits and hybrids for the readout. One side of the silicon strip sensors provides measurement of the r-ϕ position while the other side is used to determine the position in z. To better distinguish between possible tracks Layer 0,2 and 4 are rotated 90° with respect to the beam axis while Layer 1 and 3 are almost parallel to the beam pipe.

In Figure 3.12 one can see the first two layers of the SVX-II.

Intermediate Silicon Layers (ISL)

The ISL is constructed from five barrels in total, one central barrel and a pair of inner and outer barrels in forward and backward regions(see Figure 3.13). It covers the

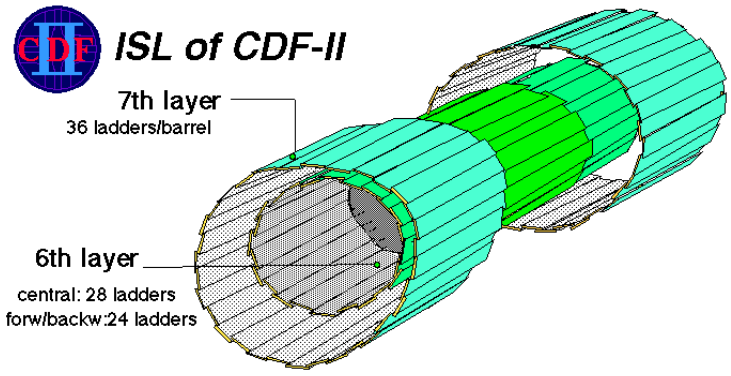

Figure 3.13: Schematic view of the ISL.

region $|\eta| < 2$ and $r = 20 - 29$ cm. The ISL silicon sensors are double-sided AC coupled micro strip detectors. The main functions of the ISL are:

- measure the particle momentum in the forward regions where the outer tracker, COT, can not fully cover
- provide anchor hit points from which track segments in SVX-II/ISL detector are searched for
- Matching of SVX-II and COT tracks through the use of ISL hitpoints

3.2.2 Drift Chamber

The Central Outer Tracker (COT) is a large open cell, cylindrical drift chamber using a read out that can record multiple hits from each sense wire.It is located within a 1.4 Tesla solenoidal magnetic field, in the radial region outside the silicon microstrip detectors and inside the time-of-flight (TOF) scintillators. It serves for the charged particle tracking at large radii in the central pseudo-rapidity region ($|\eta| < 1$). Because of its large dimensions it provides very precise momentum measurements($\sigma_{p_t}/p_t = 0.15\% \cdot p_t \cdot 1/\frac{GeV}{c}$). The COT consists of eight so called "Superlayers". The four axial layers are parallel to the beam and are responsible for the r-ϕ measurement. The rest of the eight layers, the so called stereo layers have a small stereo angle of 2° and provide the z measurement. [29]

3.2.3 Time of Flight (TOF)

The chosen TOF technique is based on plastic scintillators and photomultipliers. The primary purpose of the TOF is to provide charged kaon identification to determine the b flavor of B hadrons.

The scintillators are installed at a radius of ≈ 140 cm from the beam in the 4.7 cm of radial space between COT and the cryostat of the superconducting solenoid (see Figure 3.11). The pseudorapidity coverage of the system is roughly $|\eta| < 1$.

3.2.4 Calorimetry

In the CDF detector so-called sampling calorimeters surround the solenoid and measure the energy of all particles except muons and neutrinos. These calorimeters are made up of alternating layers of active scintillator and absorber material. A distinction is drawn between hadronic and electromagnetic calorimeters. In the former case iron is used as absorber material whereas in the latter case lead is used. In the right picture of Figure 3.10 all five calorimeters can be seen. They cover 2π in azimuthal angle ϕ and $|\eta| < 3.6$.

3.2.5 Muon System

There are a total of about 1200 muon scintillation counters in the CDF II detector. The longest (up to 320 cm) of these counters cover the central ($|\eta| < 0.6$) region and are known as the Central Scintillator Upgrade (CSP) counters. They are laid on the outside of the drift chamber of the Central Muon Upgrade (CMP) chamber stacks, behind 61 cm of steel shielding located outside the central calorimeter (see Figure 3.10). The additional shielding enables one to use CMP to confirm the hits of the innermost central muon chamber (CMU) where still many charged hadrons are present. But not only the central region of the detector is covered by muon detectors. In Figure 3.10 all other muon detectors are shown. Altogether nearly complete muon coverage up to a pseudorapidity of $|\eta| < 1.5$ is possible.

3.2.6 Trigger System

A three-level Trigger System is used at CDF to reduce the enormous amount of data generated by each beam crossing.

Level-1: The "extremely fast tracker"(XFT) forms tracks from axial hits in COT and can match these with calorimeter and muon-chamber data to form possible track candidates.

Level-2: Fast silicon tracking, calorimeter clustering . The final Level-2 decision is made in software, so more complex quantities and thresholds can be used. Also a impact parameter measurement of $35\,\mu m$ resolution is made by the Silicon Vertex Trigger (SVT).

Level-3: 250 PCs perform a full event reconstruction with two dimensional tracks and full offline type reconstruction. All events passing Level-3 are written to disk.

The collision rate is 1.7 MHz. One out of 50 events passes Level-1 so the collision rate reduces to approximately 35 kHz. This rate is further reduced by Level-2 to 700 Hz. Finally at Level-3 the final output rate is 130 Hz.

Two-Track-Trigger(TTT)

A additional description of the Two Track Trigger is appropriate because all data used within this analysis was exclusively collected by this trigger system.

Long lived particles travel a certain distance in the detector before they decay, so the production point is displaced from the decay point. The TTT scans events for long lived particles. More precisely, it searched for 2 displaced tracks with positive lifetime. The trigger criteria are:

Level-1: at least two XFT tracks with $p_t > 2$ GeV/c and $\Delta\phi < 135$ between the two momenta.

Level-2: at least two SVT tracks with $p_t > 2$ GeV/c, impact parameter d_0 between 100 μm and 2 mm, $\chi^2_{SVT} < 25$ and decay length in the x-y plane $L_{xy} > 200\mu$m.

Level-3: Refinement of track measurements. Confirmation of the Level-2 decision by checking whether p_t and d_0 requirements are still fullfilled. In a final step confirm $2 < \Delta\phi < 90$ and $L_{xy} > 200\mu m$.

Depending on different luminosity scenarios, from level-2 on additional requirements are demanded. There exist three distinct scenarios:

B_LowPt: at least two SVT tracks found and the scalar sum of the transverse momenta greater then 4.

B_Charm: requires at least two oppositely charged SVT tracks with $p_t^1 + p_t^2 > 5.5$ GeV/c.

B_HighPt: also two oppositely charged SVT tracks are needed however in the high p_t scenario the transverse momenta must satisfy $p_t^1 + p_t^2 > 6.5$ GeV/c.

4 sPlot Formalism

4.1 Motivation

Neural networks can distinguish signal from background by learning their characteristic features. Hence NeuroBayes[24], a sophisticated neural network implementation, was chosen for discriminating between $D_{s1}(2536)$ and $D_{s2}(2573)$ signal events and the enormous amount of background events produced at CDF II. The first encountered difficulty is the lack of pure signal and background samples to train the neural Network. Usually this issue is solved by training the Network with background events from sidebands and simulated signal events. Another approach, the so-called sideband-subtraction(see also Section 4.5) tries to remove the background events in the signal region by adding background events from mass sidebands which carry negative weights. If the yields are estimated correctly these events statistically compensate all background events found below the signal. The sPlot formalism[25] is a advanced sideband subtraction technique which provides binwise sideband subtraction. More generally speaking: sPlot is a statistical tool to unfold data distributions. Furthermore correct normalization and statistical uncertainties are provided by the sPlot formalism(see Section 4.4). These were the main reasons why the sPlot formalism was chosen to generate signal and background distributions for all variables used in the neural network.

4.2 Extended Likelihood Analysis

Let's suppose a sample of N events each belonging to one of n_{sp} species (e.g. signal or background events). For each event a set of variables $\vec{v} = (v_1, \ldots, v_{n_{var}})$ is measured. Given that, the distributions of these variables contain contributions of all species. The sPlot technique makes it possible to extract the distributions for each species in a given variable. This is accomplished by reweighting all events by so called sWeights ${}_s\mathcal{P}_i$ (e.g. ${}_s\mathcal{P}_{sig}$ could denote the sWeights that are used to obtain signal distributions) for a given variable.

The first step towards sPlot weights is to estimate yields N_i for each species. First a set of discriminating variables $\vec{y}$ has to be chosen. For all components of $\vec{y}$ the respective PDFs for each species have to be known. To obtain estimates for the yields an extended maximum Likelihood fit is performed. The log-Likelihood function to be minimized is

$$\mathcal{L} = \sum_{e=1}^{N} \left(\ln \left\{ \sum_{i=1}^{n_{sp}} N_i f_i(y_e, \theta_i) \right\} \right) - \sum_{i=1}^{n_{sp}} N_i, \tag{4.1}$$

where

- N is the number of events in the sample
- n_{sp} is the number of species
- N_i is an estimate for the number of events for the ith species
- y_e is the value of the discriminating variable y for event e
- f_i is the PDF of the discriminating variables y for the ith species
- θ_i is the parameter set of f_i.

N_i and θ_i are determined by the fit. Due to large sample sizes binned χ^2 fits are used to determine N_i and θ_i in Chapter 5.2.2. This decision is made because χ^2 fits are faster than Likelihood fits and does not reduce the quality of the results.

4.3 Derivation of sPlot Weights

For the probability density function of a given data sample one makes the following ansatz:

$$Nf(x,y) = \sum_{i=1}^{n_{sp}} N_i f_i(x,y) = \sum_{i=1}^{n_{sp}} N_i f_i(y) g_i(x) \; . \tag{4.2}$$

- x is the set of control variables. They are uncorrelated to y, which means that the total PDFs $f_i(x,y)$ all factorize into products $f_i(y)g_i(x)$
- y is the set of discriminating variables used in the fit
- $g_i(x)$ is the control variables' PDF for the ith species.

The aim of the sPlot analysis is to obtain distributions of control variables for different species. The expected number of events in a given x-bin with center x_c and width δx is given by

$$\langle N^{\delta x} \rangle = N \int_{-\infty}^{\infty} dy \int_{\delta x} dx f(x,y) \approx N \delta x \int_{-\infty}^{\infty} dy \int_{-\infty}^{\infty} dx f(x,y) \delta(x - x_c) \; . \tag{4.3}$$

First let's consider the case where x and y are 100% correlated. This means that x is a function of $y(x = x(y))$. x is now in the set of discriminating variables. Equation

4.3 can then be written as

$$\langle N^{\delta x}\rangle \approx N\delta x \int_{-\infty}^{\infty} dy\delta(x(y)-x_c)\int_{-\infty}^{\infty} dx f(x,y) \tag{4.4}$$

$$= N\delta x \int_{-\infty}^{\infty} dy f(y)\delta(x(y)-x_c) = N\delta x g(x_c) = \sum_{e\subset\delta x} 1\ , \tag{4.5}$$

where the following identities have been used :

$$\begin{aligned} f(y) &= \int_{-\infty}^{\infty} dx f(x,y), \text{ marginal distribution} \\ g(x) &= \int_{-\infty}^{\infty} dy f(x,y), \text{ marginal distribution} \\ \int_{-\infty}^{\infty} dy f(y)\delta(h(y)) &= \sum_i \frac{f(y_i)}{|h'(y_i)|} \text{ with } y_i \text{ being the roots of } h(y) \\ g(x) &= f(y)\left|\frac{dy}{dx}\right|, \text{ transformation law for PDFs.} \end{aligned}$$

By applying weights to each event the distribution for a species n can be reconstructed from the sole knowledge of the $f_i(y)$. This is achieved by the weight

$$\mathcal{P}_n = \frac{N_n f_n(y_e)}{\sum_k N_k f_k(y_e)}\ . \tag{4.6}$$

The calculation of the expected number of events is straightforward:

$$\langle N_n^{\delta x}\rangle \approx \delta x \int_{-\infty}^{\infty} dy \left(\sum_{i=1}^{n_{sp}} N_i f_i(y)\right)\delta(x(y)-x_c)\frac{N_n f_n(y)}{\sum_k N_k f_k(y)} \tag{4.7}$$

$$= \delta x N_n \int_{-\infty}^{\infty} dy f_n(y)\delta(x(y)-x_c) = \delta x N_n g_n(x_c) = \sum_{e\subset\delta x}\mathcal{P}_n\ . \tag{4.8}$$

For total correlation, the histograms of $g_n(x)$, called ${}_{in}\mathcal{P}lots$, give an direct estimate of the distribution $g_n(x)$, but the interpretation of ${}_{in}\mathcal{P}lots$ can lead to false assumptions for the x-distribution. As $x = x(y)$, one implicitly assumes a distribution $\hat{g}_n(x)$ for $g_n(x)$. If the fit of $f_n(y)$ is not perfect the weighted distribution will be close to $\hat{g}_n(x)$ but not necessarily close to $g_n(x)$.

Let's assume now that x is uncorrelated to y. x is a true control variable, thus no knowledge of the x-distribution enters in the definition of the weights. For equation 4.3 one obtains:

$$\begin{aligned} \langle N^{\delta x}\rangle &\approx N\delta x \int_{-\infty}^{\infty} dy f(y)\int_{-\infty}^{\infty} dx\delta(x-x_c)g(x) \\ &= \delta x \int_{-\infty}^{\infty} dy \left(\sum_{i=1}^{n_{sp}} N_i f_i(y) g_i(x_c)\right)\ . \end{aligned}$$

However, this time weighting by $\mathcal{P}_n$ does not lead to the desired result.

$$\begin{aligned} \langle N_n^{\delta x} \rangle &\approx \delta x \int_{-\infty}^{\infty} dy \left(\sum_{i=1}^{n_{sp}} N_i f_i(y) g_i(x_c) \right) \frac{N_n f_n(y_e)}{\sum_k N_k f_k(y_e)} \\ &= \delta x N_n \sum_{i=1}^{n_{sp}} g_i(x_c) \left(N_i \int_{-\infty}^{\infty} dy \frac{f_i(y_e) f_n(y_e)}{\sum_k N_k f_k(y_e)} \right) \\ &\neq \delta x N_n g_n(x_c) \; . \end{aligned} \tag{4.9}$$

Nevertheless one can simplify equation 4.9 by introducing the inverse of the covariance matrix:

$$\langle N_n^{\delta x} \rangle = \delta x N_n \sum_{i=1}^{n_{sp}} g_i(x_c) N_i \mathbf{V}_{ni}^{-1}, \text{ with} \tag{4.10}$$

$$\begin{aligned} \mathbf{V}_{ni}^{-1} &= \frac{\partial^2 (-\mathcal{L})}{\partial N_n \partial N_i} = \sum_{events} \frac{f_i(y_e) f_n(y_e)}{\left(\sum_k N_k f_k(y_e)\right)^2} \\ &\approx N \int \int dx g(x) dy f(y) \frac{f_i(y) f_n(y)}{\left(\sum_k N_k f_k(y)\right)^2} = \int dy \frac{f_i(y) f_n(y)}{\sum_k N_k f_k(y)} \; . \end{aligned}$$

Finally, the desired distribution $g_n(x_c)$ is obtained by inverting equation 4.10:

$$g_n(x_c) N_n \delta x = \sum_{i=1}^{n_{sp}} \mathbf{V}_{ni} \langle N_i^{\delta x} \rangle / N_i = \langle N^{\delta x} \rangle \sum_{i=1}^{n_{sp}} \mathbf{V}_{ni} \mathcal{P}_i / N_i \; .$$

The sWeight ${}_s\mathcal{P}_n$ for a given event e is then defined by :

$${}_s\mathcal{P}_n(y_e) = \sum_{i=1}^{n_{sp}} \mathbf{V}_{ni} \mathcal{P}_i / N_i = \frac{\sum_{i=1}^{n_{sp}} \mathbf{V}_{ni} f_i(y_e)}{\sum_{k=1}^{n_{sp}} N_k f_k(y_e)} \; . \tag{4.11}$$

4.4 Normalization and Statistical Uncertainties

To check the validity of the calculated sWeights the following normalization properties are of great use:

$$\sum_{i=1}^{n_{sp}} {}_s\mathcal{P}_i(y_e) = 1 \; \forall \text{ event } e \tag{4.12}$$

$$\sum_{e=1}^{N} {}_s\mathcal{P}_i(y_e) = N_i \; . \tag{4.13}$$

In each x-bin the statistical uncertainty on the expected number of events per species i is

$$\sigma(\langle N_i^{\delta x} \rangle) = \sqrt{\sum_{e \subset \delta x} \left({}_s\mathcal{P}_i(y_e) \right)^2} \; . \tag{4.14}$$

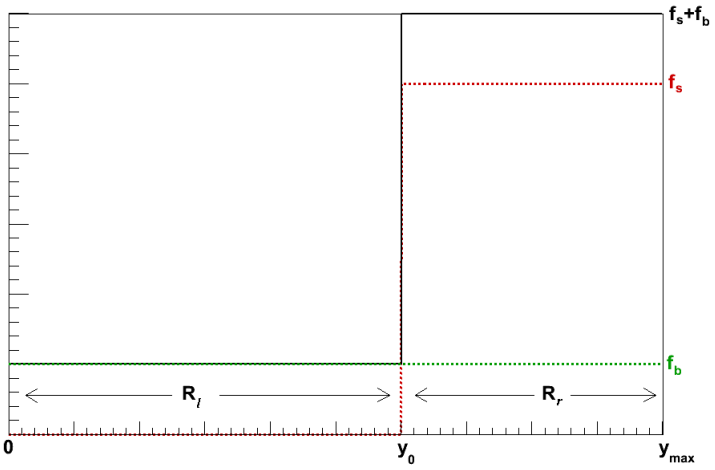

Figure 4.1: PDFs for signal and background

The covariance V_{ij} reads

$$V_{ij} = \sum_{e \subset \delta x} ({}_s\mathcal{P}_i(y_e) \cdot {}_s\mathcal{P}_j(y_e)) \tag{4.15}$$

A proof of the following equations is given in reference [25].

4.5 "Sideband Subtraction" and sPlot Formalism

In the simple case where the discriminating variable y is split in $n_y = 2$ regions and the number of species n_{sp} also equals 2, determining the sWeights is obvious. Let's consider a data sample consisting of signal and background events distributed according to the PDFs:

$$\begin{aligned} f_s &= \begin{cases} 0 & y \leq y_0 \\ \frac{1}{y_{max}-y_0} & y_0 < y \leq y_{max} \end{cases} \\ f_b &= \frac{1}{y_{max}} \,. \end{aligned}$$

In Figure 4.1 the PDFs and different regions are illustrated. One can easily express the number of signal and background events (N_s, N_b) by the number of events in regions $R_l : [0, y_0]$ and $R_r : [y_0, y_{max}]$:

$$\begin{aligned} N_l &= N \int_0^{y_0} f(y)dy = \int_0^{y_0} (N_s f_s(y) + N_b f_b(y))\, dy = N_b \int_0^{y_0} f_b(y)dy = N_b \frac{y_0}{y_{max}} \\ N_r &= N \int_{y_0}^{y_{max}} f(y)dy = (y_{max} - y_0) \left(N_s \frac{1}{y_{max} - y_0} + N_b \frac{1}{y_{max}} \right) = N_s + N_b \left(1 - \frac{y_0}{y_{max}} \right) \,. \end{aligned} \tag{4.16}$$

Solving Equation 4.16 for N_s and N_b leads directly to the weights for signal and background in the regions R_l and R_r:

$$\begin{aligned} N_b &= \frac{y_{max}}{y_0} N_l = w_b^{(l)} \cdot N_l + w_b^{(r)} \cdot N_r \\ N_s &= -\frac{y_{max} - y_0}{y_0} N_l + N_r = w_s^{(l)} \cdot N_{(l)} + w_s^{(r)} \cdot N_r \ . \end{aligned}$$

The weight for events in the region R_α of species i is w_i^α:

$$\begin{aligned} w_b^{(l)} &= \frac{y_{max}}{y_0} \\ w_s^{(l)} &= -\frac{y_{max} - y_0}{y_0} \\ w_b^{(r)} &= 0 \\ w_s^{(r)} &= 1 \end{aligned}$$

The signal distribution for a control variable x, for example, is reproduced by assigning weights to all events. Events in the region $R_{(l)}$ receive the weight $w_s^{(l)}$ whereas the rest of the events, which all belong to the region R_r , are weighted with $w_s^{(r)}$. The calculated weight w_i^α is equal to the sWeight ${}_s\mathcal{P}_i(y_\alpha)$[25].

The above derivation works for the general case where the number of species equals the number of regions($n_{sp} = n_y$). In this case the matrix equation corresponding to equation 4.16 for a histogram with n_y bins is:

$$N^\alpha = \sum_{i=1}^{n_{sp}} N_i F_i^\alpha, \tag{4.17}$$

where

- N^α is the number of events in the bin α
- N_i is the number of events for species i
- $F_i^\alpha = \int_{bin\,\alpha} f_i(y)dy$.

Now, N^α is inverted:

$$N_i = \sum_{\alpha=1}^{n_y} N^\alpha \left(F^{-1}\right)_i^\alpha = \sum_{\alpha=1}^{n_y} N^\alpha w_i^\alpha. \tag{4.18}$$

Thus the elements of F^{-1} are the weights w_i^α needed to reconstruct the PDFs of the different species.

Unfortunately for $n_y > n_{sp}$ the above procedure does not apply because 4.17 is not sufficient to determine N_i. One has to go back to the derivation given in Section 4.3. The appropriate weight can be calculated according to the sWeight denoted in equation 4.11 for continuous y. It can be shown that for continuous or binned y the sWeights reproduce on average the PDFs of the control variables x[25].

4.6 Training NeuroBayes with sPlot Weights

The sPlot formalism permits a training of the neural network with experimental data only. No simulated signal is necessary because both signal and background distributions are reconstructed by weighting all events with the appropriate sWeights. To assure a correct treatment of such a training within NeuroBayes the code of the program itself had to be adapted . The main changes are:

- Check for sPlot training: If the target has one value different from {-1,0,1} and the training is a classification then the training is treated as an sPlot training
- The target variable is set to the sWeight for signal ${}_s\mathcal{P}_{sig}$ defined by equation 4.11. In the case of a simple sideband subtraction with as many bins as species the weights defined by equation 4.18 can be used. The result is the same but the derivation is much simpler.
- Events are passed only once to the network. However, internally Neurobayes uses ${}_s\mathcal{P}_{sig}$ to reconstruct the signal distributions and ${}_s\mathcal{P}_{back} = 1 - {}_s\mathcal{P}_{sig}$ to estimate the background distributions for all input variables.
- The quadratic and the entropy error function of the neural network as well as their derivatives have been adapted. For each event there is a signal and background contribution. As an example the quadratic error function now reads :

$$E \sim \sum_{i=1}^{n_{events}} (t_i - o_i)^2 \longrightarrow E \sim \sum_{i=1}^{n_{events}} \left({}_s\mathcal{P}_{sig} \cdot (1 - o_i)^2 + {}_s\mathcal{P}_{back} \cdot (0 - o_i)^2 \right) .$$

  Here t_i is the target value for event i and o_i stands for the network output of event i.

- The calculation of the statistical uncertainties for the signal purity p_s has been adapted for sPlot training. These errors are used during preprocessing by the orthogonal polynomial fit (preprocessing flag 14) and the monotonous spline fit (preprocessing flag 15). The formulas used are derived in the next section.

4.7 Error Calculation for Training with sPlot Weights

For a given input variable x Neurobayes generates (flattened) histograms to approximate the true distributions of signal and background events.
Then the signal purity for each bin is calculated:

$$p_s\left(N_s, N_b\right) = \frac{N_s}{N_s + N_b} .$$

For an sPlot training the statistical uncertainty on p_s can be calculated by Gaussian error propagation. From now on all sums are taken over all events in one bin ($\sum \equiv$

$\sum_{e\subset\delta x}$) and $w_s(w_b)$ stands for the signal (background) sWeight, respectively. The covariance and variances for $N_s = \sum w w_s$ and $N_b = \sum w(1-w_s) = \sum w w_b$ are given by equations 4.15 and 4.14:

$$\begin{aligned} cov_{sb} &= \sum w^2 w_s w_b \\ \sigma_s^2 &= \sum (w w_s)^2 \\ \sigma_b^2 &= \sum (w w_b)^2 = \sum w^2 (1-w_s)^2 \end{aligned}$$

where w denotes an additional weight. The variance of p_s follows from Gaussian error propagation:

$$\begin{aligned} \sigma_{p_s}^2 &= \left(\frac{\partial p_s}{\partial N_s}\right)^2 \cdot \sigma_s^2 + \left(\frac{\partial p_s}{\partial N_b}\right)^2 \cdot \sigma_b^2 + 2\frac{\partial p_s}{\partial N_s}\frac{\partial p_s}{\partial N_b} cov_{sb} \\ &= \left(\frac{N_b}{(N_s+N_b)^2}\right)^2 \cdot \sigma_s^2 + \left(\frac{-N_s}{(N_s+N_b)^2}\right)^2 \cdot \sigma_b^2 + 2\left(\frac{N_b\,(-N_s)}{(N_s+N_b)^4}\right) \cdot cov_{sb}\,. \end{aligned}$$

The statistical uncertainty on p_s reads

$$\sigma_{p_s} = \frac{1}{(N_s+N_b)^2} \cdot \sqrt{N_b^2\sigma_s^2 + N_s^2\sigma_b^2 - 2N_sN_b cov_{sb}}\,.$$

In the case of sPlot training the quantity p_s and the error σ_{p_s} are passed to the fitting routines implemented in Neurobayes (individual preprocessing flag 14 and 15).

5 Analysis of $D_s^{**} \rightarrow D^0 K^+$, $D^{*0} K^+$

Because the CDF Run-II detector was not designed to detect low energy neutral particles, the decays which include a D^{*0} appear in the $D^0 K^+$ mass spectrum. Hence the decays

$$\begin{aligned} D_{s1}(2536) \rightarrow D^{*0} K^+ \rightarrow \quad & D^0 \pi^0 K^+ \rightarrow \quad K \pi \pi^0 K^+ \\ \ldots \rightarrow \quad & D^0 \gamma K^+ \rightarrow \quad K \pi \gamma K^+ \end{aligned}$$

and

$$D_{s2}^*(2573) \rightarrow D^0 K^+ \rightarrow K \pi K^+$$

are seen simultaneously since neither neutral pions nor photons are reconstructed.

5.1 Data Collection and Preselection Requirements

The data used in this analysis was exclusively collected by the so-called Two Track Trigger (see section 3.2.6). Pion and kaon tracks are matched in a vertex fit to obtain D^0 candidate events. In a next step the reconstructed D^0 mesons are combined with all remaining tracks to form the D_s^{**} candidates. For analysis data collected from February 2002 to January 2007, corresponding to an integrated luminosity of 1.6 fb^{-1} is used. This enormous amount of data is reduced by demanding preselection requirements which allow to analyze the data set in a more efficient way. Nevertheless it has to be guaranteed that basically only background events are removed. The requirements are:

- At least 2 hits in the silicon system for each track
- At least 10 hits in the Central Outer Tracker for each track
- $Q < 0.641$ GeV/c^2 which corresponds to $m_{re}\left(D_s^{**}\right) < 3$ GeV/c^2. Q is defined as $Q = m_{re}\left(D_s^{**}\right) - m_{re}\left(D^0\right) - m_{pdg}\left(K\right)$
- $\left|m_{re}(D^0) - m_{pdg}(D^0)\right| < 0.032$ GeV/c^2

where m_{re} denotes reconstructed masses and m_{pdg} are world averages from the Particle Data Group [3]. Additionally the reflection $D^{*\pm} \rightarrow D^0 \pi^\pm$ can be removed by an appropriate requirement on the corresponding Q-value:

- $Q_{D^*} > 0.01$GeV/c^2, where $Q_{D^*}$is the Q-value for pion mass hypothesis of the Kaon from the D_s^{**}. $Q_{D^*} = m_{re}\left(D^{*\pm}\right) - m_{re}\left(D^0\right) - m_{pdg}\left(\pi\right)$

$D^{*\pm}$ is seen in the $D^0 K$ mass spectrum due to wrong kaon identification. The kaon which is combined with the D^0 to form a D_s^{**} candidate, could as well be a pion. This leads to the four-vector of D_s^{**} being calculated with the wrong mass hypothesis for the kaon since the particle in reality is a pion. Now the very narrow $D^{*\pm}$ is seen as a broad resonance in the $D^0 K^+$ mass spectrum. A recalculation of the mass with pion mass hypothesis reveals the narrow $D^{*\pm}$ state (see left plot in Figure 5.1).

Additionally $D_1 \to D^{*0}\pi$ and $D_2^* \to D^0 \pi$ are seen in the Q_{D^*} spectrum where they appear as relatively broad resonances with much background below them (see Figure 5.2). In the $D^0 K$ spectrum they will be even broader. Therefore no further requirements are necessary.

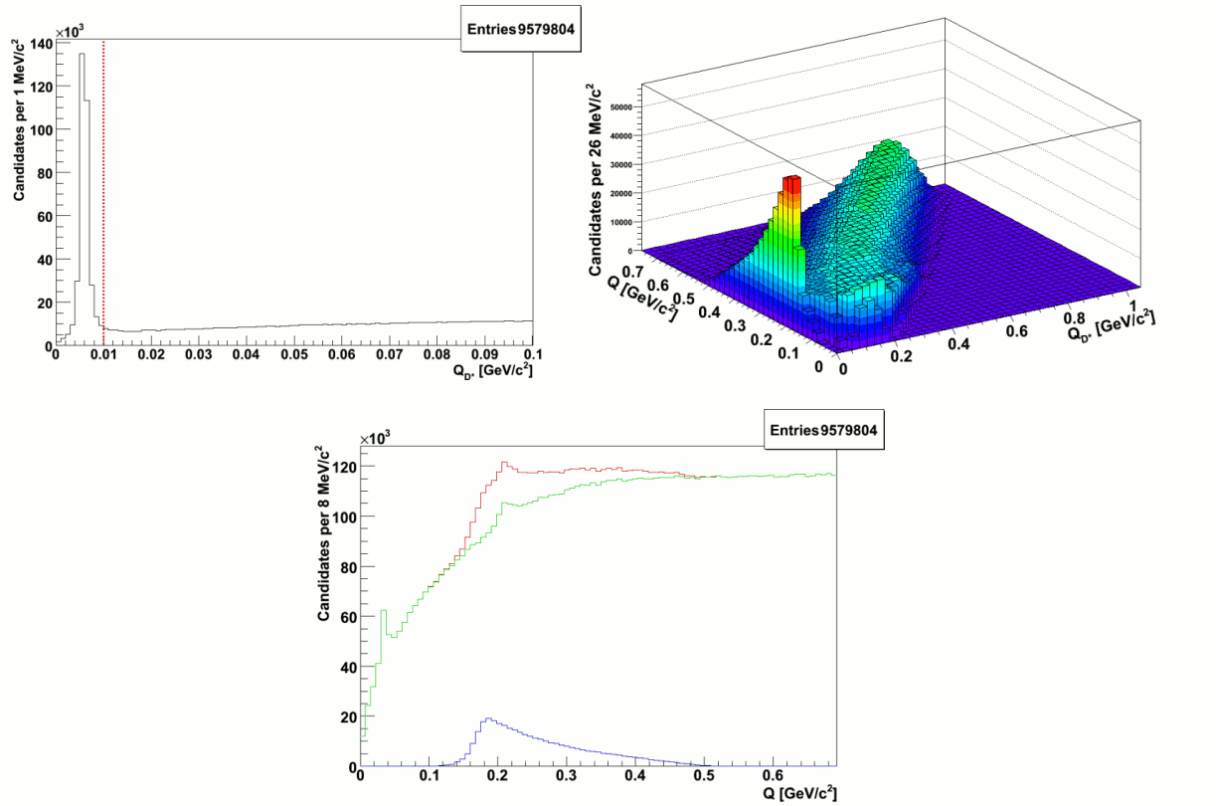

Figure 5.1: Plots to illustrate the $D^{*\pm}$ reflection in the $D^0 K$ mass spectrum. The left figure shows the $D^{*\pm}$ state where the mass was recalculated with pion mass hypothesis. The dotted red line indicates the position of the cut. On the right side the correlation between the old and the recalculated Q-value is shown in a so called lego plot. The reflection can be seen very clearly at low Q_{D^*} values. The histograms below show the, in this case, broad $D^{*\pm}$ resonance (blue), the $D^0 K$ spectrum with (red) and without the reflection (green).

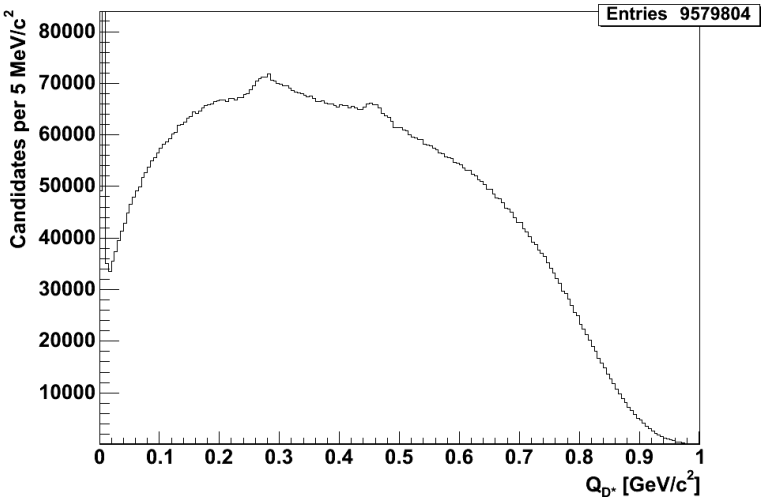

Figure 5.2: The reflections $D_1 \rightarrow D^{*0}\pi$ and $D_2^* \rightarrow D^0\pi$ are seen at $Q_{D^*} = 0.274$ GeV/c^2 and $Q_{D^*} = 456$ GeV/c^2, respectively.

5.2 Combined Training on $D_{s1}(2536)$ and $D_{s2}(2573)$

5.2.1 Mass Dependence in the Sample

Because sPlot training is a sophisticated sideband subtraction training it is essential to check whether the desired variables show any mass dependence or not. Only if the discriminating variables are not correlated with the control variables the sPlot subtracted distributions for signal and background are consistent with the true PDFs within the statistical uncertainties. Here the control variables are the variables used for the training. To locate mass dependent variables, a NeuroBayes density training for the Q-value distribution in the region $Q \in \{0, 0.64\}$ is chosen. 1 Million events are randomly chosen out of the ones remaining after the above preselection. Like expected, all transverse momenta and all pseudorapidities show significant mass dependence. Especially the transverse momentum $p_t(K(D_s^{**}))$ of kaon originating from the D_s^{**} is strongly mass dependent and its correlation propagates to the kaon ratio which is one of the best discriminating variables available. The kaon ratio is the likelihood ratio for kaon identification based on TOF and dE/dx (energy loss per unit length) information.

One could now think of two possible scenarios :

1. The correlation can be removed and the decorrelated variable is used for the training.

2. The variable has to be dismissed because there is no obvious way to get ride of the mass dependence.

To remove most of the correlation to the Q-value the selection requirements are tightened. This is possible without loosing a significant amount of signal events. The following list summarizes the additional requirements:

- $p_t(K(D_s^{**})) > 1.2$ GeV/c
- $K_{ratio}(K(D_s^{**})) > 0.06$
- number of COT axial hits for $K(D_s^{**})$ greater equal 35
- number of COT stereo hits for $K(D_s^{**})$ greater equal 30.

Figure 5.3 illustrates the effect of the requirements on p_t. The plots are made on a signal enriched subsample with 350000 events. In the left figure events with high kaon ratio form a narrow horizontal band over the whole Q-region whereas in the right plot this band is not present. This is achieved without destroying the vertical signal bands at $Q_{D_{s1}} = 0.035$ and $Q_{D_{s2}} = 0.214$.

More quantitative results are summarized in Table A.2 where the correlation of all variables before and after the selection is compared. They are sorted according to their correlation to the Q-value. All variables marked with an "x" are removed from the training set. The last four variables in Table A.2 are as well mass dependent although the Neurobayes preprocessing fit could not describe their dependence.

It has to be pointed out that mass dependence of a sample will always distort the PDFs used for training. Nevertheless if correlations can be eliminated from the sample, all remaining variables are available for training. For a training with simulated events the selection also depends on whether the variables are correctly modeled or not. Now one has to balance the reasons for the different approaches and pick the one suitable for the specific problem.

5.2.2 Fitting the $D^0 K^+$ Spectrum

In order to calculate appropriate sPlot weights for the $D^0 K^+$ spectrum a binned χ^2 fit is performed to determine the yields as well as the PDFs for signal and background. Out of the remaining approximate 11 Million events 4 Million are randomly chosen to represent the whole sample. The following functions are used to model the distributions for signal and background events

$$
\begin{aligned}
f\left(Q,\theta_s,\theta_b\right) &= N \cdot \left(r_s f_s\left(Q,\theta_s\right) + r_b f_b\left(Q,\theta_b\right)\right) \\
f_b\left(Q,\theta_b\right) &= n_{f_b} \cdot \left(Q^{\alpha} e^{-\beta x} + Q^{\gamma} e^{-\delta x} + G(\mu,\sigma)\right) \\
f_s\left(Q,\theta_s\right) &= r_{s1} f_{s1} + \left(1 - r_{s1}\right) f_{s2} = r_{s1}\left(r_{\pi^0} f_{\pi^0} + \left(1 - r_{\pi^0}\right) f_{\gamma}\right) + \left(1 - r_{s1}\right) f_{s2} \\
f_{\pi^0}\left(Q,\mu,\sigma\right) &= n_G G(Q,\mu,\sigma) \\
f_{\gamma}\left(Q,\alpha,\beta,\gamma\right) &= \frac{1}{\gamma-\beta}\left(\frac{1}{1+e^{-\alpha(Q-\beta)}} + \frac{1}{1+e^{\alpha(Q-\gamma)}} - 1\right) \\
f_{s2}\left(Q,\mu_{BW},\Gamma_{BW}\right) &= n_{BW}(Q_0,Q_{max}) \cdot BW(Q,\mu_{BW},\Gamma_{BW})
\end{aligned}
$$

with

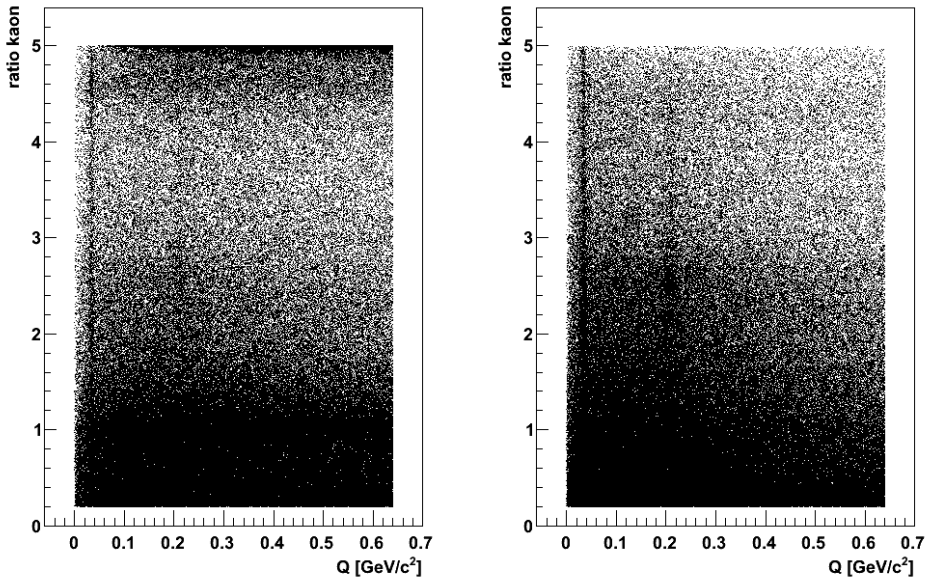

Figure 5.3: Correlation between $K_{ratio}(K(D_s^{**}))$ and the Q-value before(left) and after the cut on $p_t(K(D_s^{**}))$(right).

- $\theta_s = \{r_{\pi^0}, \mu, \sigma, \alpha, \beta, \gamma, n_{BW}\}$ being the parameter set for signal
- $\theta_b = \{n_{f_b}, \alpha, \beta, \gamma, \delta, \mu, \sigma\}$ being the parameter set for background
- $f_{s1/s2}$ the PDFs for $D_{s1}(2536) \rightarrow D^{*0}(2007)K$ and $D_{s2}(2573) \rightarrow D^0K$,respectively
- $f_{\pi^0/\gamma}$ the PDFs for fraction of f_{s1}, where the D^{*0} decays into $D^0\pi^0$ and $D^0\gamma$, respectively
- $BW(\mu_{BW}, \Gamma_{BW})$, a Breit Wigner function with mean μ_{BW} and width Γ_{BW}
- $n_{BW}(Q_0, Q_{max}) = 1./\int_{Q_0}^{Q_{max}} BW(Q; \mu_{BW}, \Gamma_{BW})dQ$, the normalization for a Breit Wigner function for the interval $[Q_0, Q_{max}]$
- G a Gaussian function with standard deviation σ and mean μ. n_G is the normalization
- r_s, r_{s1}, r_{π^0} all being fractions between $[0, 1]$ which determine the contributions of the corresponding PDFs
- N the number of all events in the sample.

The result of the binned χ^2 fit is shown in Figure 5.4.

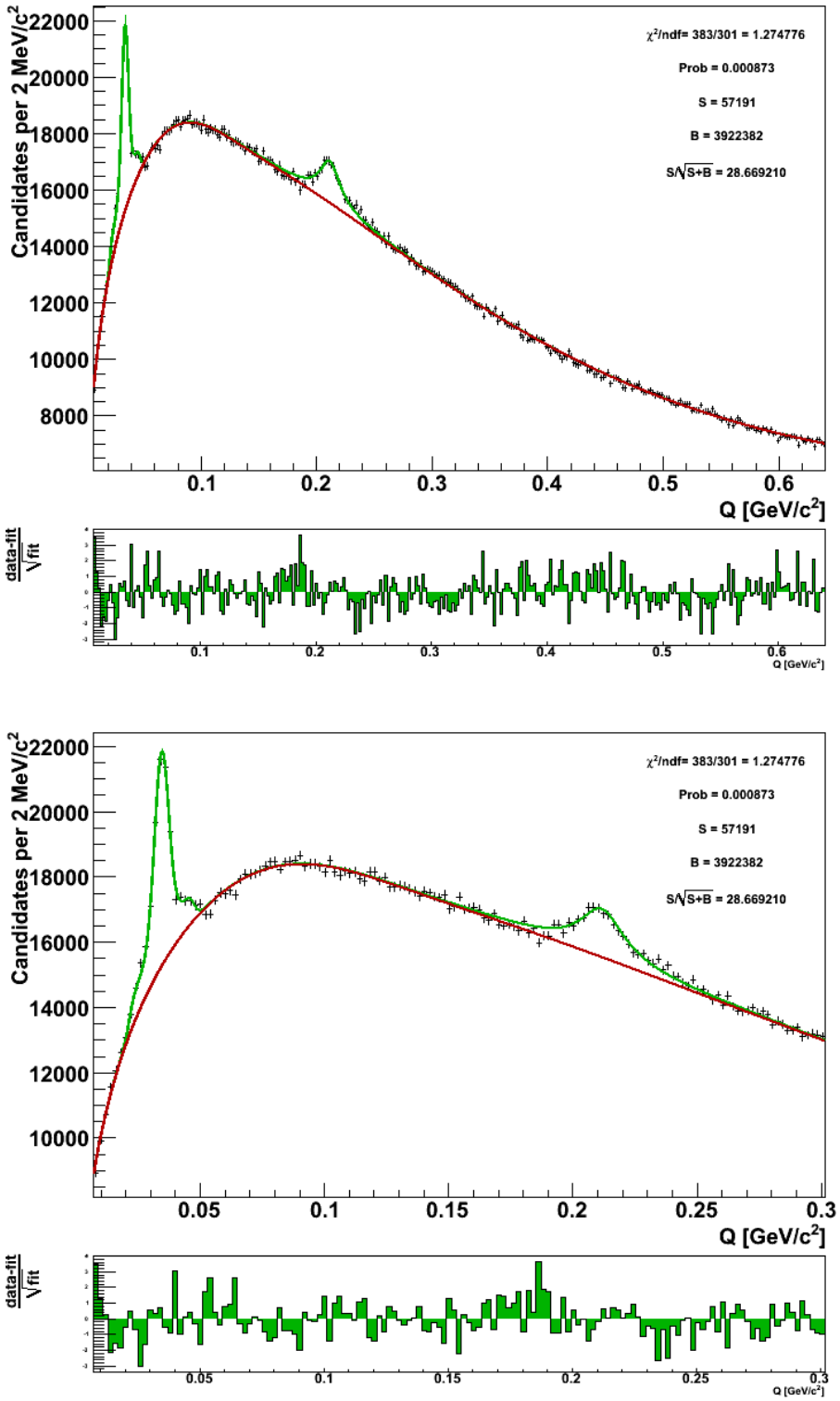

Figure 5.4: Fit used to determine θ_s and θ_b. In the above plot the region $Q = (0.007 - 0.64)$ GeV/c^2 is shown. Below a zoom in the region $Q = (0.007 - 0.3)$ GeV/c^2 is shown. The green curve shows $f(Q, \theta_s, \theta_b)$ and the background $f_b(Q, \theta_b)$ is drawn in red.

5.2.3 Neurobayes Configuration, Variables for the Training

As stated in Chapter 4 an estimate for the true distribution of species i can be constructed by histograming all events of the sample with the sPlot weight w_i for a given control variable x. This is exactly what Neurobayes does: It uses the provided sPlot weights to create the histograms for signal and background of all input variables. These weights are calculated according to equation 4.11 by using the parameters and PDFs determined in the previous section. To assure their validity it is checked whether equations 4.12 and 4.13 hold.

Finally, a Neurobayes training with 4 Million events is performed. Table A.3 summarizes the properties of the training set. Variables with an additional significance less than three sigma have not been used.

5.2.4 Training Results

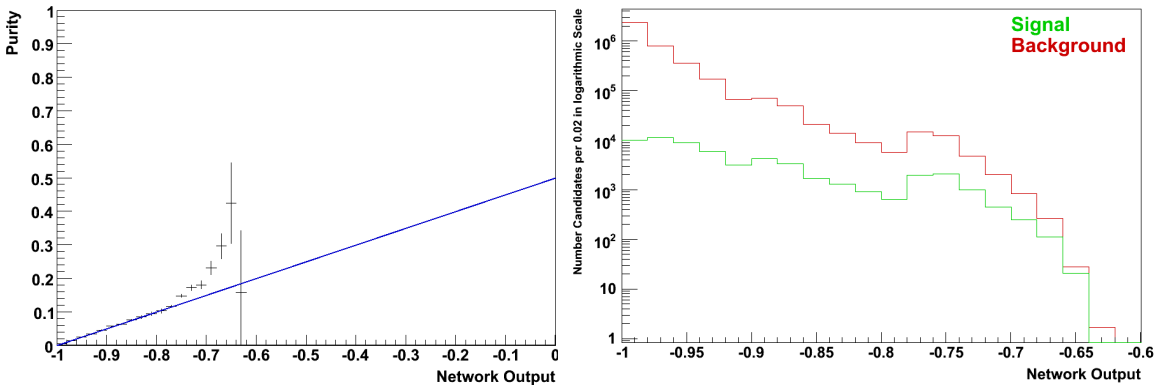

Figure 5.5: Purity as a function of the neural network Output(left). Histograms for signal (green) and background (red) for different Network Outputs(right).

In all plots "purity" stands for the signal purity $p_s = N_s/N$ with N_s being the number of signal events. The purity histogram (see Figure 5.5) is diagonal for Network Outputs less than -0.76. For higher values deviations from the diagonal can be seen which remain significant although the statistical uncertainties become larger. However, these comprise to less than one per cent of the data. For all plots (5.5,5.6,A.3) the statistical uncertainties of the purity have been calculated using equation 4.14. In the left plot of Figure 5.5 the calculations of the correct error had to be redone after the training.

To illustrate the validity of the sPlot formalism one can compare the generated distributions with the physically expected ones. This is done for the D^0 mass and lifetime distributions. The corresponding distributions are shown in Figure 5.6.

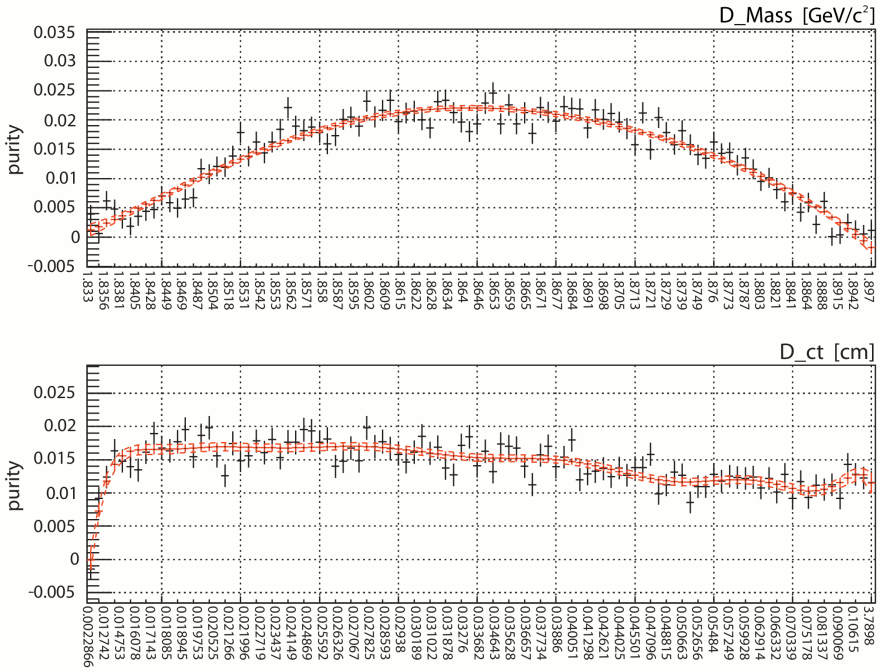

Figure 5.6: Signal Purity as a function of D^0 Mass(top) and $c\tau_{D^0}$(bottom).

Both distributions nicely show the expected behavior. The mass distribution has its maximum at the world average of 1.865 GeV and decreases symmetrically until it reaches signal purity $\hat{p}_s = 0$ in the sideband region of the D^0 mass distribution. For the lifetime, $\hat{p}_s$ decreases rapidly for small values as expected for a mean lifetime of $\tau_{D^0} = (410.1 \pm 1.5) \times 10^{-15}$ s which equals $c\tau_{D^0} = 0.01229$ cm. The rest of the purity plots can be found in the Appendix (Figure A.3)

The plots in figures 5.6 and A.3 show few bins with negative $\hat{p}_s$. Since negative weights are allowed and necessary it is possible that negative $\hat{p}_s$ occur due to statistical fluctuations. It is important to note that this is only the case for the estimated $\hat{p}_s$ and not for the true signal probability. The model holds as long as $\hat{p}_s$ is consistent with zero. However, if $\hat{p}_s$ lies systematically below zero the considered variable is probably mass dependent.

5.2.5 Optimization of the Signal Significance

The chosen requirements on the neural network output has to maximize the number of signal events N_s. However at the same time the statistical uncertainty of all events $N = N_s + N_b$ should be small. This can be achieved by maximizing the signal significance S defined as

$$S = \frac{N_s}{\sqrt{N_s + N_b}} .$$

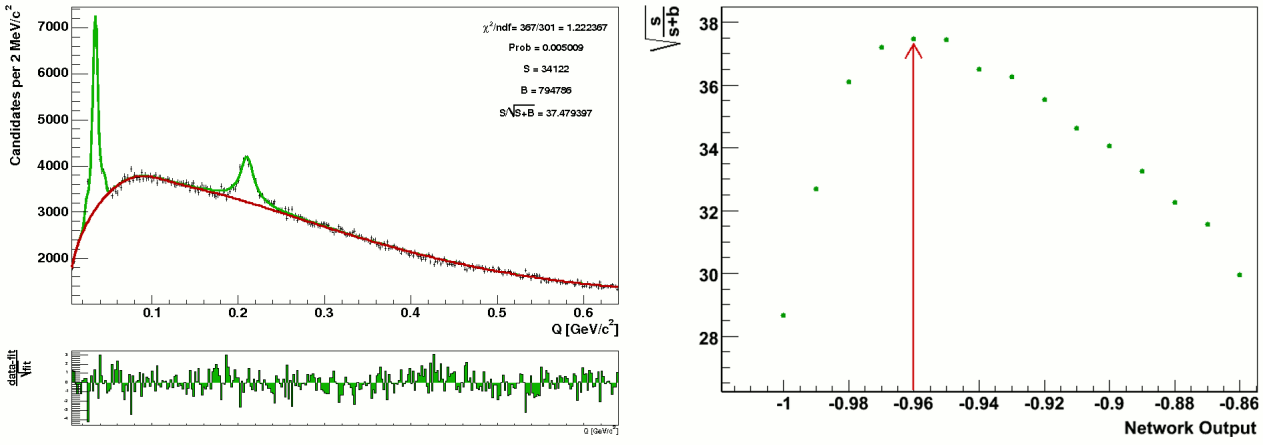

Figure 5.7: In the left figure the fit result for maximum significance is shown. In the right figure the red arrow marks this value along with the corresponding network output.

Because the true values N_s and N_b are unknown a fit has been performed for different neural network cuts to estimate them. Then the estimated $\hat{N}_s$ and $\hat{N}_b$ are used to calculate S. In Figure 5.7 the left plot shows the fit for the maximum significance $S = -0.96$ for the 4 million training events.

6 Measurements

6.1 Search for Broad Resonances

Due to the width of $\Gamma_{D_{sJ}(2700)} = 110 \pm 27$ MeV [3] no pronounced peak is expected. In addition the large background produced in an hadron collider makes it very difficult to detect such broad resonances. The chance to see $D_{sJ}(2860)$ is slightly better because its width is $\Gamma_{D_{sJ}(2860)} = 48 \pm 17$ MeV [3]. The states are expected at $Q = 0.34$ GeV/c^2 ($D_{sJ}(2700)$) and $Q = 0.5$ GeV/c^2 ($D_{sJ}(2860)$). Inspecting the Q spectrum for different network cuts two broad states emerge at the expected positions (see Figure 6.1).

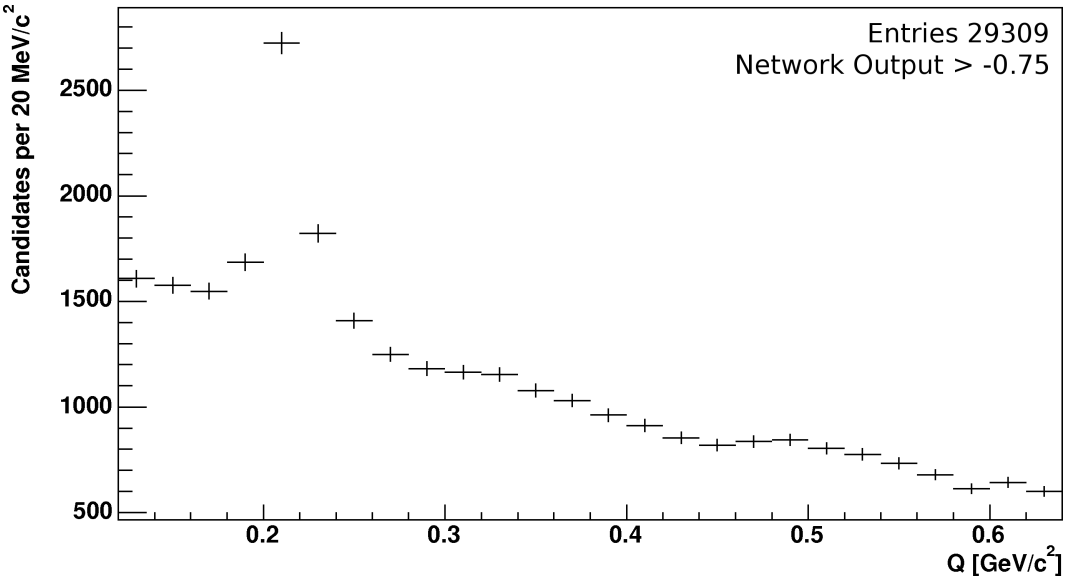

Figure 6.1: $D_{s2}(2573)$ together with $D_{sJ}(2700)$ and $D_{sJ}(2860)$

In order to demonstrate that the data is compatible with the results from Belle [2] and BaBar [1] it has been fitted with the following parametrization:

$$
\begin{aligned}
Nf(x;\theta) &= N\left(r_s f_s\left(x,\theta_s\right) + r_b f_b\left(x,\theta_b\right)\right) \\
f_b &= r_b x^{\alpha} e^{-\beta x} \\
f_s &= \left(1 - r_{2700} - r_{2860}\right) \cdot BW\left(x;\mu_{2573},\Gamma_{2573}\right) + \\
&\quad r_{2700} \cdot BW(x;\mu_{2700},\Gamma_{2700}) + \\
&\quad r_{2860} \cdot BW(x;\mu_{2860},\Gamma_{2860}) \ .
\end{aligned}
$$

where

- N is the number of events
- r_i is a fraction between zero and one for the particle of species i
- $f_{s/b}$ are the PDFs for signal and background, respectively
- $BW(x;\mu,\Gamma)$ is a Breit Wigner function normalized to the interval $Q \in [0.12, 0.64]$ with mean μ and width Γ.

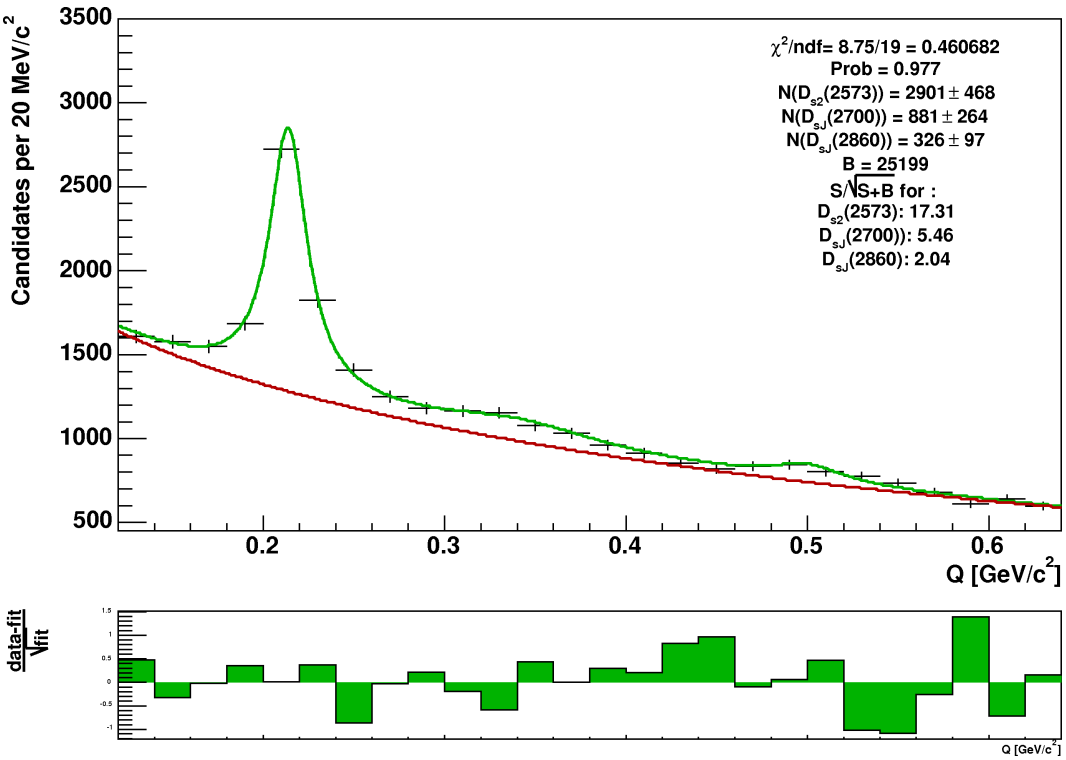

Figure 6.2: $D_{s2}(2573)$ together with $D_{sJ}(2700)$ and $D_{sJ}(2860)$

For this fit mean values and widths are fixed to the world averages. The errors for the yields are determined by Gaussian error propagation including the correlations between different fractions.

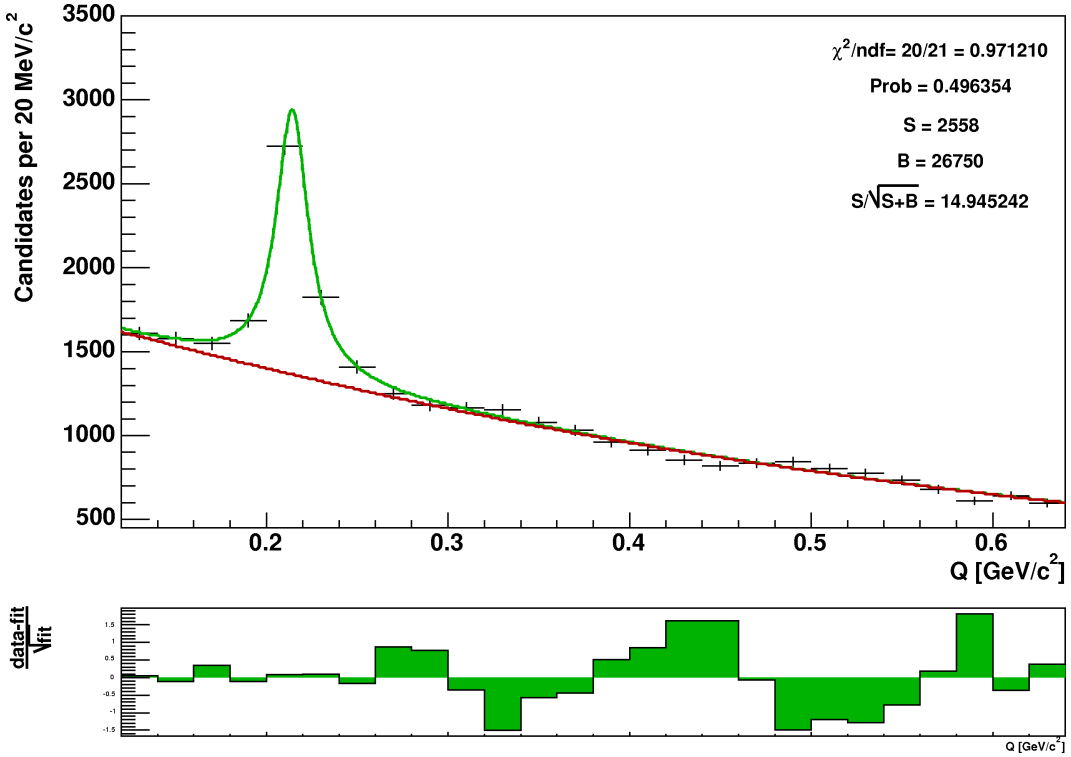

Figure 6.3: D^0K spectrum without the broad resonances $D_{sJ}(2700)$ and $D_{sJ}(2860)$.

The results is convincing, although this does not imply that other parametrizations could not describe the data as good as the one chosen above. To test an alternative hypothesis, only $D_{s2}(2573)$ is used to describe the signal. The parametrization for the background is the same and for $D_{s2}(2573)$ one Breit Wigenr function normalized to $Q \in [0.12, 0.64]$ is used(see Figure 6.3).

It can be stated that the fit without a parametrization for the broad states accurately describes our data. However, one can see systematic deviations in the region where these states are expected. This means that our data is compatible with the measured results from Belle and BaBar but not statistically significant.

6.2 Analysis of D_{s1} (2536)

This Section is exclusively reserved for the analysis of $D_{s1}(2536)$, denoted as D_{s1} in the following. The decays considered are:

$$D_{s1} \to D^{*0}K^+ \to \quad D^0\pi^0K \tag{6.1}$$

$$\ldots \to \quad D^0\gamma K^+ \tag{6.2}$$

The significance optimized data used for the following measurements is shown in Figure 6.4. The mass line shape of D_{s1} now depends on two different aspects. On the

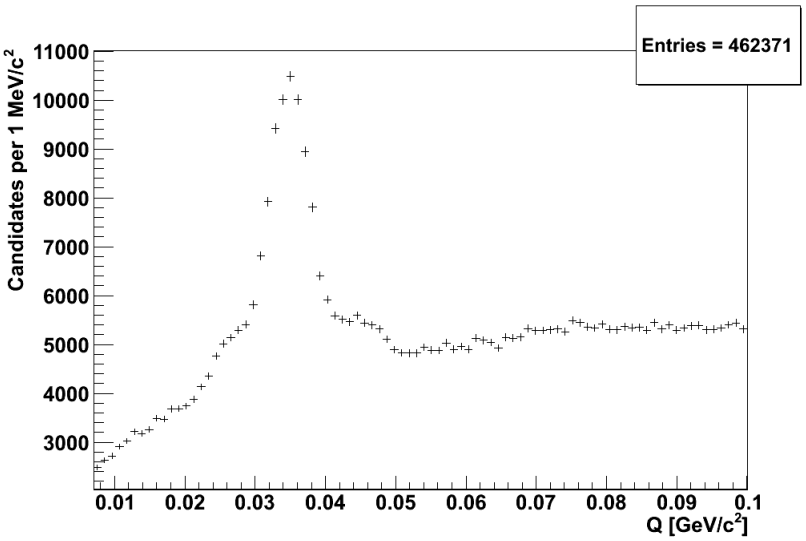

Figure 6.4: Significance optimized D_{s1} signal

one hand it is important whether D^{*0} decays over a pion (narrow peak in Figure 6.4) or a photon (broad structure in Figure 6.4). This dependence allows a measurement of the branching ratio $\Gamma_{\pi^0\gamma} = \Gamma(D^0\pi^0)/\Gamma(D^0\gamma)$. On the other hand angular distributions influence the mass line shape. These distributions depend on three further parameters: the ratio of D- and S-wave amplitudes $|D/S|$, the phase ϕ_{DS} between D- and S-wave and ρ_{00}, the probability that D_{s1} has helicity 0. If D_{s1} is produced unpolarized ($\rho_{00} = 1/3$) $|D/S|$ can only be determined as a function of the phase ϕ_{DS}. However, the amplitude ratio $R_\Lambda = |A_{10}|^2 / |A_{00}|^2$ can be determined without referring to a phase.

In order to model the angular dependence a Monte Carlo simulation, assuming phase space decay, is generated. Then the same preselection requirements as for the real data sample are applied. By reweighting simulated D_{s1} signal events it is possible to generate candidate histograms for different values of $|D/S|$, ϕ_{DS} and ρ_{00}. The reweighting is done in every iteration of a binned χ^2 minimization which has the simulated candidate histograms and the real data as input. Hence this fit can be used to determine $\Gamma_{\pi^0\gamma}$ and R_Λ.

As a first step the angular distributions are derived using the helicity formalism.

6.2.1 Angular Distributions

The decays in 6.1 have the following form:

$$\begin{aligned} 1 &\rightarrow 23 \\ 2 &\rightarrow 45, \end{aligned} \tag{6.3}$$

where the number in Equation 6.3 refer to the corresponding particles. The helicity formalism is especially suited to describe such sequential two body decays. Contrary to the partial wave formalism which uses spin components, helicities are used to model the dynamics of the decays. One advantage of this formalism is that decays like $1 \to 23$ can be measured within one reference frame. In addition the derivation of the angular distributions is easier because less sums appear in the formulas.

To describe sequential two body decays like 6.3 the following parameters are necessary:

- helicities of all particles $\lambda_1 - \lambda_5$
- angles $\Omega = (\theta, \phi)$ defined in the unprimed coordinate system $X = (x, y, z)$
- angles $\Omega' = (\theta', \phi')$ defined in the primed coordinate system $X' = (x', y', z')$

The unprimed coordinate system X is the rest frame of particle 1 with spin quantization axis (z) chosen parallel to its momentum in the lab-frame ($\vec{p}_1^{lab}$). θ and ϕ are defined by the flight direction of particle 2 in X. To obtain X the lab-frame is rotated by $R(\phi_1^{lab}, \theta_1^{lab}, -\phi_1^{lab})$ where R is an Euler rotation that rotates the z^{lab} axis onto the flight direction of particle 1.

In order to describe the second decay one has to perform a second rotation and an additional boost to get from the X-frame to the X'-frame. First the unprimed axes are rotated by $R(\phi, \theta, -\phi)$, then the system is boosted into the rest frame of particle 2 to define the primed system. The primed system X' is the rest frame of particle 2 with spin quantization axis z' along the momentum $\vec{p_2}$ in the unprimed system. Thus θ' and ϕ' are just the angles defined by the flight direction of particle 4 in the primed system. In Appendix A Figure A.4 shows the distributions for all angles.

6.2.2 Derivation of the angular distributions

The amplitude for the process in 6.1 reads

$$A\left(\Omega, \Omega'; \lambda_1, \lambda_3, \lambda_4, \lambda_5\right) = \sqrt{\frac{(2s_1+1)}{4\pi}} \sqrt{\frac{(2s_2+1)}{4\pi}} \sum_{\lambda_2} D^{s_1 *}_{\lambda_1, \lambda_2 - \lambda_3}(\Omega)\, A_{\lambda_2 \lambda_3} D^{s_2 *}_{\lambda_2, \lambda_4 - \lambda_5}(\Omega')\, B_{\lambda_4 \lambda_5}$$

where s_1 and s_2 denotes the spins of particle 1 and particle 2 respectively. The Wigner functions $D^s_{\lambda,\lambda'}$ functions can be expressed by

$$D^s_{\lambda,\lambda'}(\alpha, \beta, \gamma) = e^{-i\alpha\lambda} d^j_{\lambda\lambda'}(\beta)\, e^{i\gamma\lambda'}$$

where the $d^j_{\lambda\lambda'}(\beta)$ functions are tabulated, for example, in the Particle Data Book. To obtain the angular distribution one has to square the amplitude and sum over

spins,

$$I(\Omega,\Omega') = \frac{1}{\Gamma_1\Gamma_2}\frac{2s_1+1}{4\pi}\frac{2s_2+1}{4\pi}\sum_{\lambda_1\lambda_1'\lambda_2'\lambda_2\lambda_3\lambda_4\lambda_5}\rho_{\lambda_1\lambda_1'} \tag{6.4}$$

$$\left\{D^{s_1}_{\lambda_1,\lambda_2-\lambda_3}(\Omega)\,D^{s_1*}_{\lambda_1',\lambda_2'-\lambda_3}(\Omega)\,A^*_{\lambda_2\lambda_3}A_{\lambda_2'\lambda_3}D^{s_2}_{\lambda_2,\lambda_4-\lambda_5}(\Omega')\,D^{s_2*}_{\lambda_2',\lambda_4-\lambda_5}(\Omega')\,B^*_{\lambda_4\lambda_5}B_{\lambda_4\lambda_5}\right\}$$

where A and B denote the helicity amplitudes for the first $(1\to 23)$ and the second $(2\to 45)$ decay respectively. Γ_1 is the decay rate for the first decay: $\Gamma_1 = \sum_{\lambda_2\lambda_3}|A_{\lambda_2\lambda_3}|^2$ and Γ_2 is the decay rate for the second decay: $\Gamma_1 = \sum_{\lambda_4\lambda_5}|B_{\lambda_4\lambda_5}|^2$.

Now let's evaluate 6.4 for the decays

$$D_{s1}\to D^{*0}K^+\to \quad D^0\pi^0K \tag{6.5}$$

$$\ldots\to \quad D^0\gamma K^+. \tag{6.6}$$

Since they differ only from each other in the neutral particle equation 6.4 can be partly evaluated leaving the helicity $\lambda_5 = \lambda_{\pi^0/\gamma}$ indetermined. After substituting $\chi = \phi' - \phi$ and integrating over ϕ Equation 6.4 reads

$$\begin{aligned}
&I(\theta,\theta',\chi) \propto \frac{1}{\Gamma}\frac{9}{8\pi}\sum_{\lambda_5} \\
&|A_{10}|^2\,\frac{1}{4}\left(\rho_{00}\left(1-3cos^2\theta\right)+\left(1+cos^2\theta\right)\right)\left[\left(d^1_{1,-\lambda_5}\right)^2+\left(d^1_{-1,-\lambda_5}\right)^2\right]+ \\
&|A_{10}|^2\,\frac{1-3\rho_{00}}{2}sin^2\theta cos2\chi\cdot d^1_{-1,-\lambda_5}d^1_{-1,-\lambda_5}+\frac{sin\theta cos\theta}{\sqrt{2}}\frac{1-3\rho_{00}}{2}\cdot \\
&\left[d^1_{-1,-\lambda_5}d^1_{0,-\lambda_5}\left(A^*_{10}A_{00}e^{i\chi}+A_{10}A^*_{00}e^{-i\chi}\right)-d^1_{-1,-\lambda_5}d^1_{0,-\lambda_5}\left(A^*_{10}A_{00}e^{i\chi}+A_{10}A^*_{00}e^{-i\chi}\right)\right]+ \\
&|A_{00}|^2\left(d^1_{0,\lambda_5}\right)^2\cdot\left(\rho_{00}cos^2\theta+\frac{1-\rho_{00}}{2}sin^2\theta\right)
\end{aligned} \tag{6.7}$$

where all d-functions depend on θ'. For the first decay $(D_{s1}\to D^{*0}K)$ there are three helicity amplitudes $A_{10}=A_{-10}$, and A_{00} corresponding to the possible helicities of particle 2. In the second decay($D^{*0}\to D^0\pi^0$ or $D^{*0}\to D^0\gamma$) there exists one independent helicity amplitude which cancels out with Γ_2. Hence the total decay rate reads $\Gamma = \sum_{\lambda_1}|A_{\lambda_10}|^2 = 2|A_{10}|^2+|A_{00}|^2$.

Now let's consider the angular distribution for the decay

$$D_{s1}\to D^{*0}K^+\to D^0\pi^0K.$$

Since π^0 is a scalar particle its helicity λ_5 equals 0 . This simplifies Equation 6.7

$$\begin{aligned}
I(\theta,\theta',\chi) \quad\propto\quad & \frac{1}{\Gamma}\frac{9}{8\pi}\Bigg\{|A_{10}|^2\,\frac{sin^2\theta'}{4}\left(\rho_{00}\left(1-3cos^2\theta\right)+\left(1+cos^2\theta\right)\right) \\
&-\frac{1}{4}|A_{10}|^2\left(1-3\rho_{00}\right)sin^2\theta sin^2\theta' cos2\chi \\
&+\mathcal{RE}\left(A^*_{10}A_{00}\right)\left(1-3\rho_{00}\right)sin\theta cos\theta sin\theta' cos\theta' cos\chi \\
&+|A_{00}|^2\,\frac{cos^2\theta'}{2}\left(\left(1-cos^2\theta\right)-\rho_{00}\left(1-3cos^2\theta\right)\right)\Bigg\}
\end{aligned} \tag{6.8}$$

which can further be further simplified by assuming unpolarized D_{s1}:

$$I\left(\theta,\theta',\chi\right) = I\left(\theta'\right) \propto \frac{1}{\Gamma}\frac{3}{8\pi}\left(\left|A_{10}\right|^2 sin^2\theta' + \left|A_{00}\right|^2 cos^2\theta'\right). \tag{6.9}$$

So for an unpolarized initial state the angular distributions $I(\theta)$ and $I(\chi)$ are flat. If the helicity amplitudes are equal ($|A_{10}| = |A_{00}|$) no angular dependence is seen at all.

For the decay

$$D_{s1} \to D^{*0}K^+ \to D^0\gamma K.$$

one expects a different angular dependence since the photon is a massless spin-1 particle which can be circularly polarized but not longitudinally, so $\lambda_5 = \pm 1$ and equation 6.7 reads now

$$\begin{aligned} I\left(\theta,\theta',\chi\right) \propto \frac{1}{\Gamma}\frac{9}{8\pi}\Bigg\{ & \left|A_{10}\right|^2 \frac{\left(1+cos^2\theta'\right)}{4}\left(\rho_{00}\left(1-3cos^2\theta\right)+\left(1+cos^2\theta\right)\right) \\ & +\frac{1}{4}\left|A_{10}\right|^2\left(1-3\rho_{00}\right)sin^2\theta sin^2\theta' cos2\chi \\ & -\mathrm{Re}\left(A_{10}^* A_{00}\right)\left(1-3\rho_{00}\right)sin\theta cos\theta sin\theta' cos\theta' cos\chi \\ & +\left|A_{00}\right|^2\frac{sin^2\theta'}{2}\left(\left(1-cos^2\theta\right)-\rho_{00}\left(1-3cos^2\theta\right)\right)\Bigg\} \end{aligned} \tag{6.10}$$

and for the unpolarized case one obtains

$$I\left(\theta,\theta',\chi\right) = I\left(\theta'\right) \propto \frac{1}{\Gamma}\frac{3}{8\pi}\left(\left|A_{10}\right|^2\left(1+cos^2\theta'\right)+\left|A_{00}\right|^2 sin^2\theta'\right). \tag{6.11}$$

6.2.3 Relation to partial wave amplitudes

The helicity amplitudes and partial wave amplitudes are related by the following equations

$$A_{10} = \frac{1}{\sqrt{3}}\left(S+\frac{D}{\sqrt{2}}\right); \qquad A_{10} = \frac{1}{\sqrt{3}}\left(S-\sqrt{2}D\right) \tag{6.12}$$

$$\begin{aligned} D/S &= \sqrt{2}\frac{z-1}{1+2z} = \sqrt{\Gamma_D/\Gamma_S}e^{i\phi_{DS}} \\ z &= A_{10}/A_{00} = \sqrt{R_\Lambda}e^{i\phi_{10}} \\ |D/S|^2 &= \frac{2\left(\left(2R_\Lambda - \sqrt{R_\Lambda}cos\phi_{10}-1\right)^2+\left(3\sqrt{R_\Lambda}sin\phi_{10}\right)^2\right)}{\left(4R_\Lambda+4\sqrt{R_\Lambda}cos\phi_{10}+1\right)^2} \end{aligned} \tag{6.13}$$

with

- $\Gamma_{D/S}$ being the width for the D- (S-) wave contribution, respectively
- ϕ_{10} being the phase between the helicity amplitudes A_{10} and A_{00}.

	Partial wave basis				Helicity basis				Ref.
	$\frac{\Gamma_D}{\Gamma_{tot}}$	$\frac{\Gamma_S}{\Gamma_{tot}}$	$\left\|\frac{D}{S}\right\|^2$	ϕ_{DS}	$\frac{\|A_{10}\|^2}{\Gamma_{tot}}$	$\frac{\|A_{00}\|^2}{\Gamma_{tot}}$	R_Λ	ϕ_{10}	
Pure S-wave	0	1	0	undef.	1/3	1/3	1	0	Fig.6.7, Fig.6.5a+f, Fig.6.6a+f
"Pure" $\|A_{10}\|^2$	1/3	2/3	1/2	0	1	0	∞	undef.	Fig.6.9, Fig.6.5c+h, Fig.6.6c+h
"Pure" $\|A_{00}\|^2$	2/3	1/3	2	π	0	1	0	undef.	Fig.6.10, Fig.6.5d+i, Fig.6.6d+i
Pure D-wave	1	0	∞	undef.	1/6	2/3	1/4	π	Fig.6.11, Fig.6.5e+j, Fig.6.6e+j

Table 6.1: Connection between helicity basis and partial wave basis for all relevant quantities in the decay $D_{s1} \to D^{*0}K$.

From now on an unpolarized initial state $D_{s1}(2536)$ is assumed and Equations 6.9 and 6.11 are used to model the angular dependence.

It follows that only $R_\Lambda = |A_{10}|^2 / |A_{00}|^2$ can be measured. A additional measurement of the phase ϕ_{10} would be necessary to calculate Γ_D/Γ_{total}, the D-wave contribution to the total width. However, there are four possible values of R_Λ (see Table 6.1) for which no measurement of the phase is needed to calculate Γ_D/Γ_{total}. For these values a comparison of the simulated angular distributions with the observed data enables one to make qualitative statements about the assumptions for Γ_D/Γ_{total} . For all other values of R_Λ the phase ϕ_{10} has to be known in order to calculate Γ_D/Γ_{total}. Nevertheless for unknown ϕ_{10} upper and lower bounds can be calculated.

6.2.4 Discussion of different D-wave Contributions to the total Width in the Decay $D_{s1} \to D^{*0}K$

Recently the Belle collaboration published a result for the ratio of D- and S-wave amplitudes of $D/S = (0.63 \pm 0.07 \pm 0.02) \cdot \exp(\pm i\,(0.76 \pm 0.03 \pm 0.01))$[4] measured in the decay mode $D_{s1} \to D^* K^0_s$. This corresponds to a D-wave contribution to the width of $\Gamma_D/\Gamma_{total} = |D/S|^2 / \left(1 + |D/S|^2\right) = 0.28$ which is contrary to the HQET predictions. The corresponding angular distributions for the decays $D_{s1} \to D^{*0}K \to D^0\gamma K$ and $D_{s1} \to D^{*0}K \to D^0\pi^0 K$ are shown in Figure 6.5b) and Figure 6.5g) . The remaining plots in Figures 6.5 are referenced in Table 6.1 where more information about amplitudes and phases is summarized. They illustrate how the shape of the angular distributions changes for different Γ_D/Γ_{total}.

In Figure 6.6 the Q-value distributions for the decays $D_{s1} \to D^{*0}K \to D^0\gamma K$ and $D_{s1} \to D^{*0}K \to D^0\pi^0 K$ are shown. They reflect how the angular distributions in

Figure 6.5 influence the mass line shape. This relationship will be exploited in Section 6.3 to measure R_Λ and $\Gamma_{\pi^0\gamma} = \Gamma(D^*(2007)^0 \to D^0\pi^0)/\Gamma(D^*(2007)^0 \to D^0\gamma)$. One has to remember that only for the values of R_Λ shown in Table 6.1 Γ_D/Γ_{total} can be calculated without a measurement of the phase ϕ_{10}.

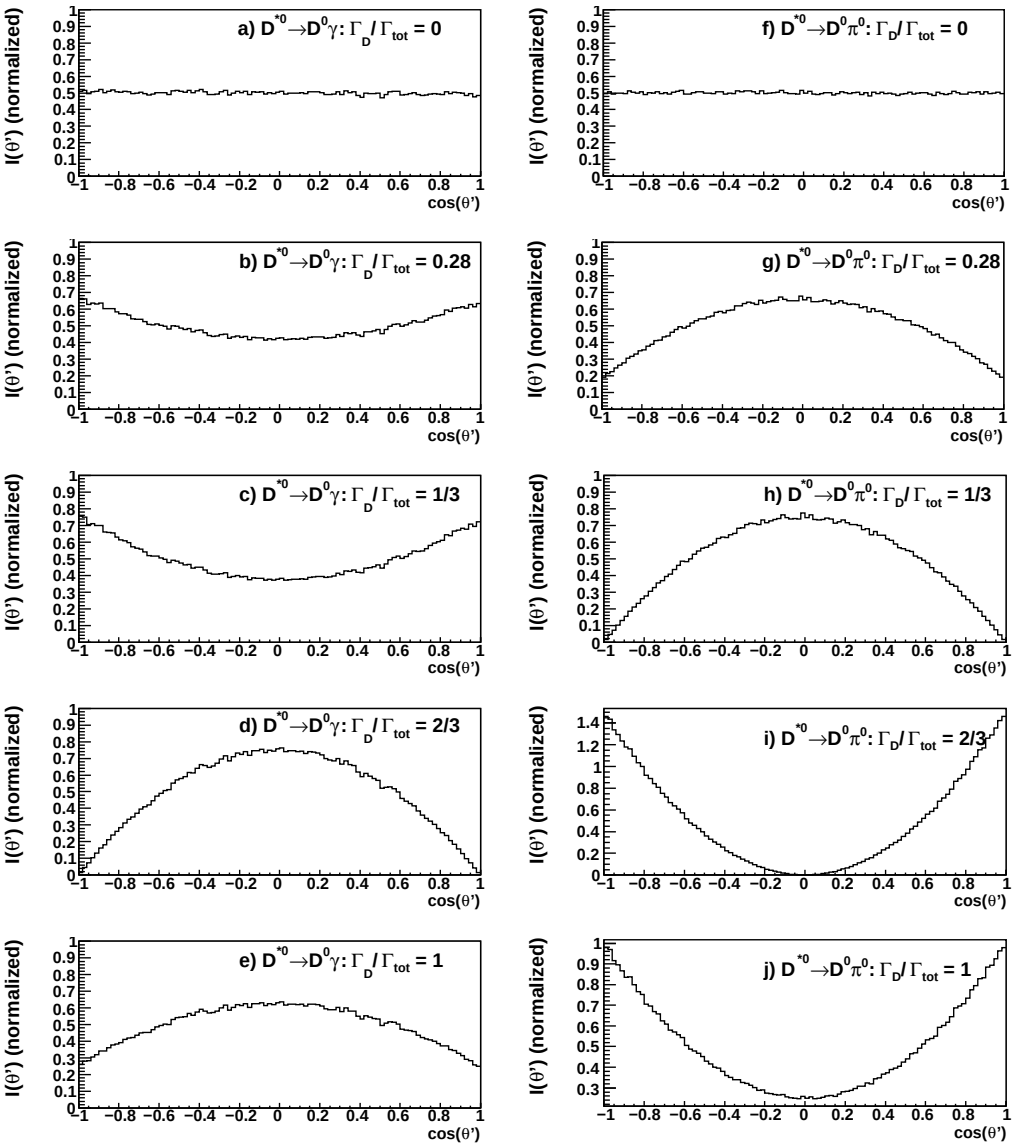

Figure 6.5: Angular distributions for different D-wave contributions to the total width Γ_D/Γ_{tot} in the decays $D_{s1} \to D^{*0}K \to D^0\gamma K$ (left) and $D_{s1} \to D^{*0}K \to D^0\pi^0 K$ (right).

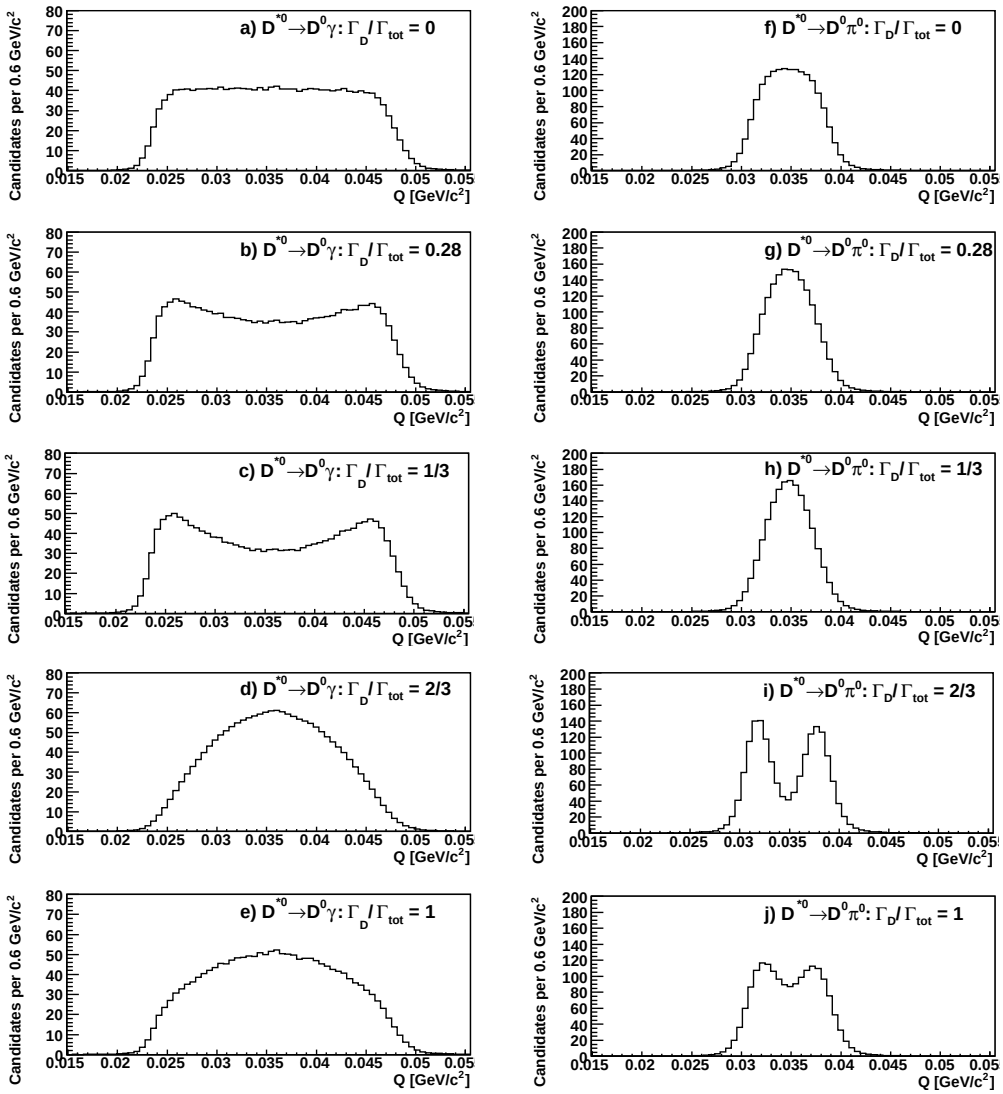

Figure 6.6: Q-value distributions for different D-wave contributions to the total width Γ_D/Γ_{tot} in the decays $D_{s1} \to D^{*0}K \to D^0\gamma K$ (left) and $D_{s1} \to D^{*0}K \to D^0\pi^0 K$ (right).

All histograms in Figure 6.5 and 6.6 were generated by the following steps:

1. Event generation by a Monte Carlo simulation assuming phase space decay
2. Reweighting of the simulated events by weights calculated by Equation 6.9 and

6.11

Having understood the relationship between the mass line shape of the decay $D_{s1} \rightarrow D^{*0}$ and its angular distributions different assumptions for Γ_D/Γ_{total} can be compared to real data.

Finally for all values of R_Λ shown in Table 6.1 and for the measured value by Belle ($R_\Lambda = 3.6 \pm 0.3 \pm 0.1$) the following function is fit to data:

$$\begin{aligned} Nf(x,\theta) &= (1-r_s)f_b + r_s \cdot f_s \\ f_s &= \left(\frac{1-r_{D_{s2}}}{1+\Gamma_{\pi^0\gamma}} \left(\Gamma_{\pi^0\gamma} \cdot h_{\pi^0}(x_i, R_\Lambda) + h_\gamma(x_i, R_\Lambda) \right) + r_{D_{s2}} G(x,\mu,\sigma) \right), \\ f_b &= n_{f_b} \cdot \left(x^\alpha e^{-\beta x} + x^\gamma e^{-\delta \cdot x} \right) \end{aligned} \tag{6.14}$$

where

- N is the number of events
- $r_s \in \{0,1\}$ is the signal fraction
- $\Gamma_{\pi^0\gamma}$ is the branching ratio $\Gamma(D^0\pi^0)/\Gamma(D^0\gamma)$
- $h_{\pi^0/\gamma}$ are normalized histograms of the simulated decays $D^{*0} \rightarrow D^0\pi^0$ and $D^{*0} \rightarrow D^0\gamma$, respectively.

The Q-value histograms h_{π^0} and h_γ contain roughly 500000 and 300000 D_{s1} signal events respectively. The results of the fits are depicted in Figures 6.7,6.8,6.9,6.10 and 6.11.

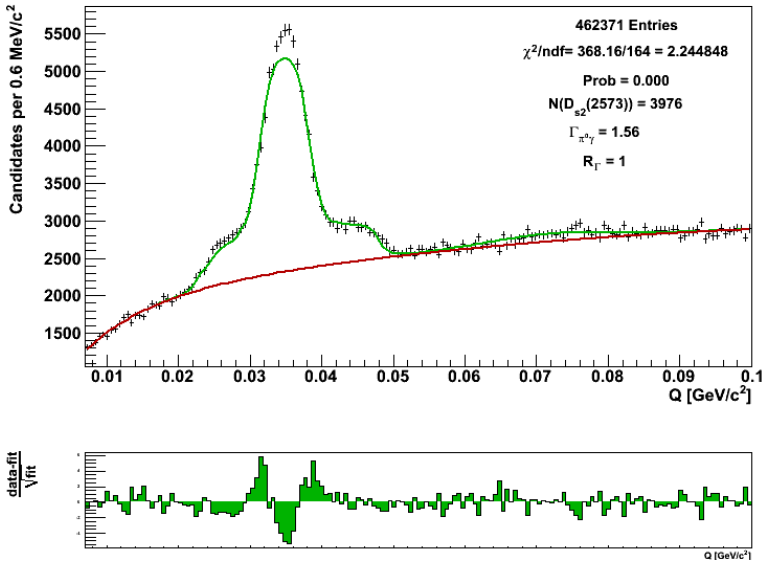

Figure 6.7: Comparison of simulated data and real data for a pure S-wave in the decay $D_{s1} \to D^{*0}K$.

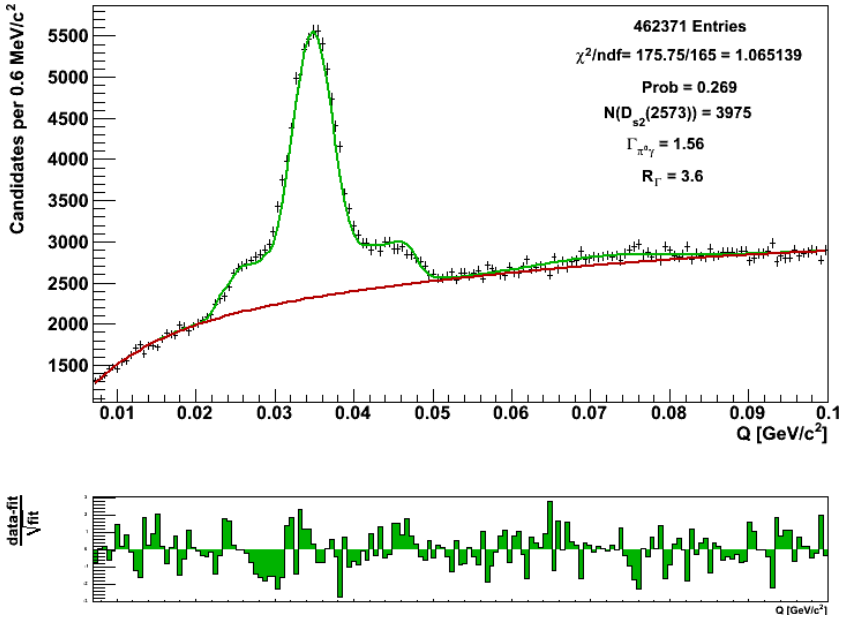

Figure 6.8: Comparison of simulated data and real data for a D-wave contribution of $\Gamma_D/\Gamma_{tot} = 0.28$ in the decay $D_{s1} \to D^{*0}K$. This corresponds to the Belle measurement of the D- and S-wave ratio $D/S = (0.63 \pm 0.07 \pm 0.02) \cdot \exp(\pm i\,(0.76 \pm 0.03 \pm 0.01))$[4].

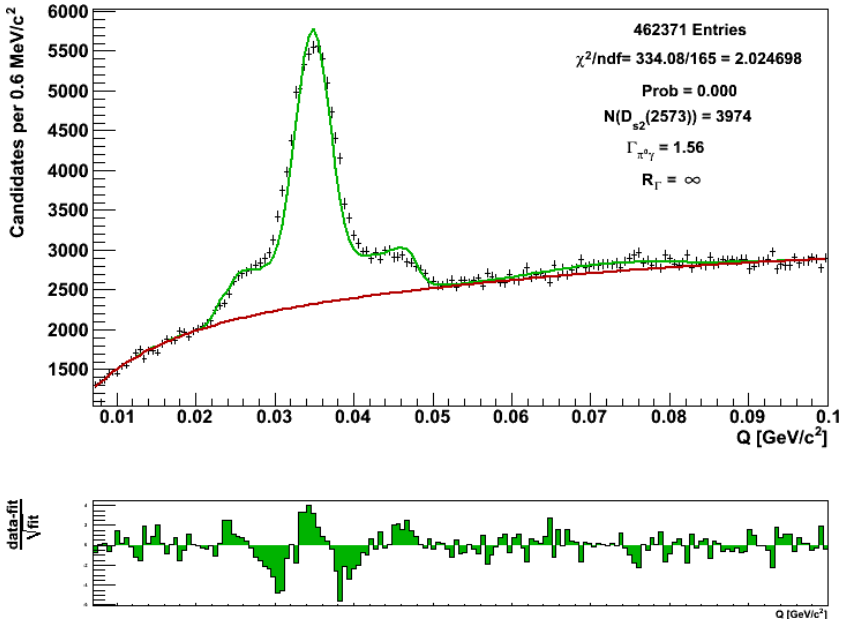

Figure 6.9: Comparison of simulated data and real data for a D-wave contribution of $\Gamma_D/\Gamma_{tot} = 1/3$ in the decay $D_{s1} \to D^{*0}K$.

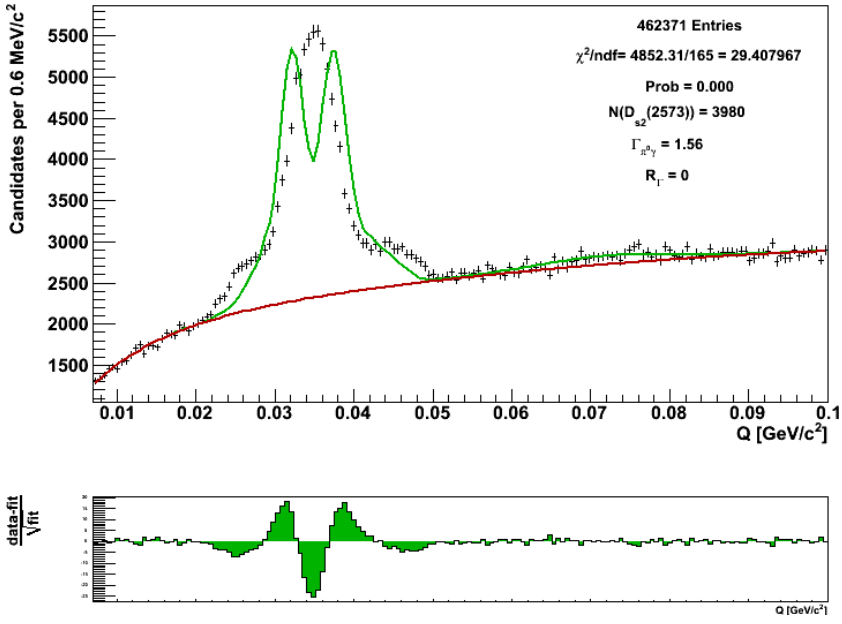

Figure 6.10: Comparison of simulated data and real data for a D-wave contribution of $\Gamma_D/\Gamma_{tot} = 2/3$ in the decay $D_{s1} \to D^{*0}K$.

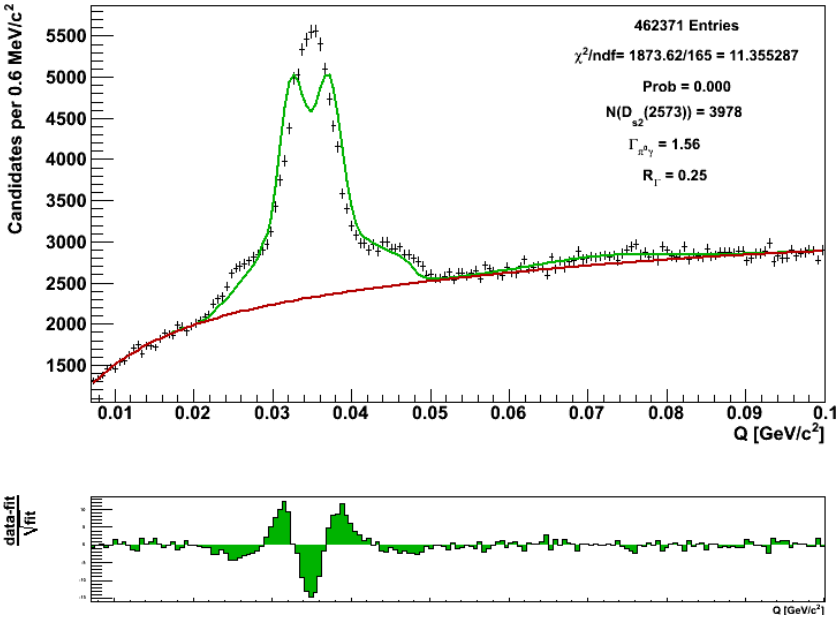

Figure 6.11: Comparison of simulated data and real data for a pure D-wave decay $D_{s1} \to D^{*0}K$.

The HQET hypothesis of a pure D-wave decay (see Figure 6.11) is the second worst fit result with an $\chi^2/ndf \approx 11$. Only the fit with $|A_{10}| = 0$ (Figure 6.10) gives a much worse result: $\chi^2/ndf \approx 29$. The rest of the fits (Figure 6.9 and Figure 6.7) are able to describe the data quite well, especially the Belle result [4] of $R_\Lambda = 3.6$ has a fit probability of $p_{Belle} = 0.269$ (Figure 6.8). This means that the HQET hypothesis of a pure D-wave decay is not consistent with the data presented in this thesis whereas the Belle result for the ratio of helicity amplitudes $R_\Lambda = 3.6$ gives a good description of the data.

6.3 R_Λ and Branching Ratio $\Gamma_{\pi^0\gamma}$ Measurement

To measure the branching ratio $\Gamma_{\pi^0\gamma}$ the above fit is repeated with parameter limits accounting for physical boundaries. The branching ratio $\Gamma_{\pi^0\gamma}$ is found to be

$$\Gamma_{\pi^0\gamma} = \frac{\Gamma(D^*(2007)^0 \to D^0\pi^0)}{\Gamma(D^*(2007)^0 \to D^0\gamma)} = 1.57 \pm 0.06.$$

what corresponds to a branching fraction Γ_{π^0} for $D^{*0} \to D^0\pi^0$ of $\Gamma_{\pi^0} = 0,611 \pm 0.0093$ assuming that $\Gamma_{total} = \Gamma_{\pi^0} + \Gamma_\gamma$ holds. The corresponding fit result is shown in Figure 6.12. This measurement of $\Gamma_{\pi^0\gamma}$ is consistent with the BarBar measurement of $\Gamma_{\pi^0\gamma} = 1.74 \pm 0.02 \pm 0.13 \Leftrightarrow \Gamma_{\pi^0} = 0.635 \pm 0.003 \pm 0.017$ [5] if additional systematic uncertainties would have been included. The systematic uncertainties can result from:

1. To small samples of simulated events which were used to account for the angular distributions
2. Different selection efficiencies for $D_{s1} \to D^{*0}K \to D^0\gamma K$ and $D_{s1} \to D^{*0}K \to D^0\gamma K$

The ratio of helicity amplitudes squared $R_\Lambda = |A_{10}|^2 / |A_{00}|^2$ was measured to be:

$$R_\Lambda = 2.65 \pm 0.24$$

Hence, our measurement is consistent with the result of Belle[4], $R_\Lambda = 3.6 \pm 0.3 \pm 0.1$, if the above systematic effects would be included.

In addition the decay $D_{s2}(2573) \to D^{*0}K^+$ is included in the fit model. Mean and standard deviation of the Gaussian are fixed to the corresponding world averages. $D_{s2}(2573) \to D^{*0}K^+$ is expected at $Q = 0.072$ GeV/c^2 and has a width of $\Gamma_{D_{s2}} = 20$MeV. Until now it has not be seen in the decay mode $D^{*0}K^+$ although this is physically not forbidden. In Figure 6.12 $D_{s2}(2573)$ is seen at $Q = 0.072$. Finally Figure 6.13 shows the angular distributions as well as the histograms $h_{\pi^0/\gamma}$ for $R_\Lambda = 2.65$.

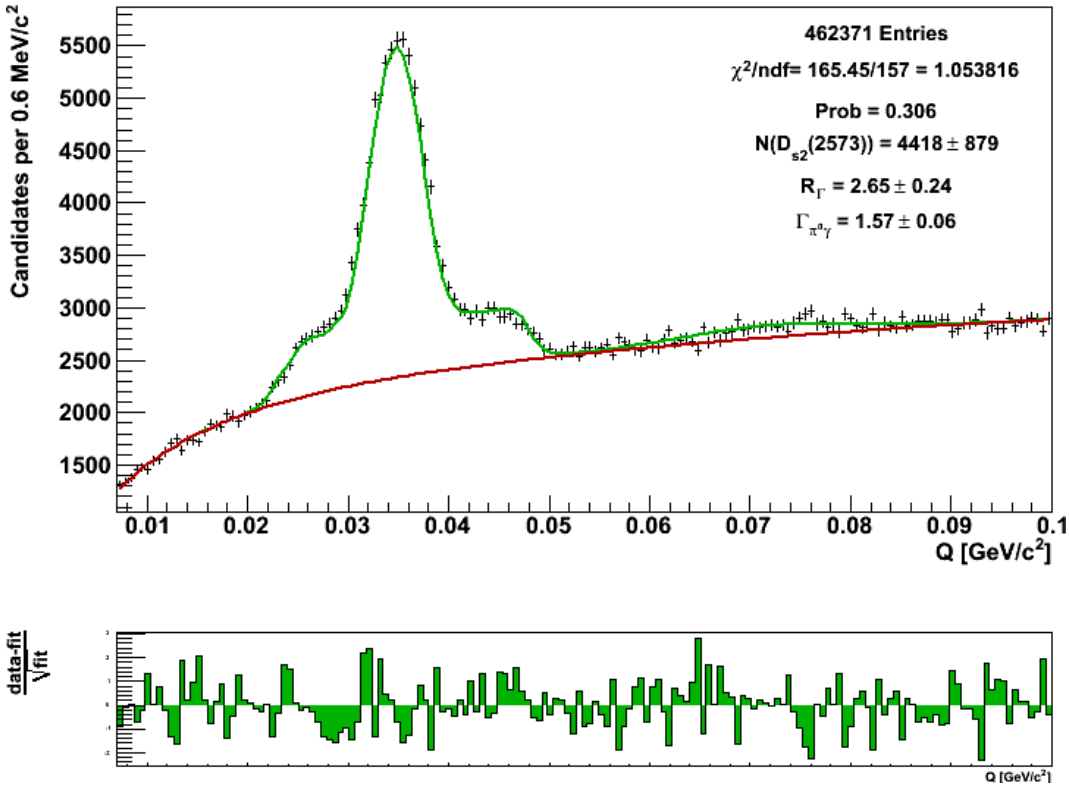

Figure 6.12: Measurement of $D^*(2007)^0 : \frac{\Gamma(D^0\pi^0)}{\Gamma(D^0\gamma)}$ and R_Λ.
At $Q = 0.072$ GeV/c^2 the decay $D_{s2}(2573) \to D^{*0}K^+$ is seen. The prominent signal at the left was used to measure $\Gamma_{\pi^0\gamma}$.

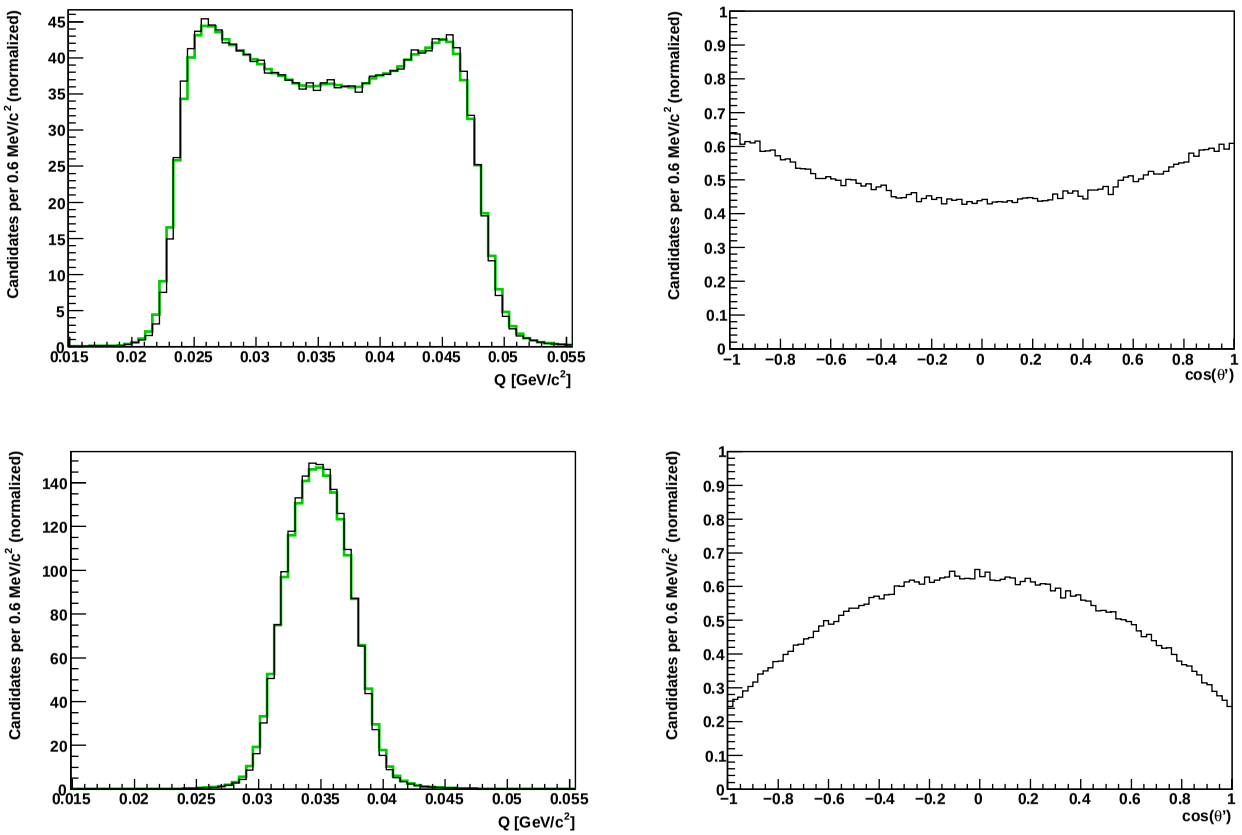

Figure 6.13: In Figures a) and c) the simulated distributions of the Q-value and the helicity angle for the decay $D_{s1} \rightarrow D^{*0}K \rightarrow D^0\gamma K$ are shown respectively. In Figures b) and d) the corresponding distributions for the decay $D_{s1} \rightarrow D^{*0}K \rightarrow D^0\pi^0 K$ are depicted. The green histograms in Figures a) and b) are smoothed, whereas the black histograms show the original data. For smoothing a weighted mean over five bins was used. (For $R_\Lambda = 2.65$).

7 Conclusion and Outlook

Five years after BarBar's discovery of the enigmatic $D_{s0}(2317)$[33] the majority of model predictions (see Table 2.2) for the masses of $D_{s0}(2317)$ and $D_{s1}(2460)$ are approximately 100 MeV too high. Further, these states are expected to be broad resonances which contradicts experimentally determined widths of less than 4 MeV for both states[6]. These discrepancies make heavy quark spectroscopy in the D_s^{**} sector to a promising field of research for applying new statistical methods which can help to find broad D_s^{**} states.

To obtain the following results the features of a new statistical technique, the so called sPlot method were exploited to allow NeuroBayes trainings without the need of Monte Carlo models. The sPlot method is an advanced background-subtraction formalism for which the NeuroBayes package was adapted to make background-subtracted trainings possible. With the help this analysis method and the data collected at the CDF II detector many qualitative results were possible.

For analysis the D^0K mass spectrum was used. Clear evidence for the decays $D_{s1}(2536) \rightarrow D^{*0}K$ and $D_{s2}(2573) \rightarrow D^0K$ could be found. $D_{s1}(2536)$ can be seen as an reflection in the D^0K mass spectrum since the CDF II detector was not designed to detect low energetic neutral particles. Hence, a measurement of the branching ratio $\Gamma_{\pi^0\gamma} = \Gamma(D^*(2007)^0 \rightarrow D^0\pi^0)/\Gamma(D^*(2007)^0 \rightarrow D^0\gamma)$ seems hardly possible. Nevertheless, by exploiting the mass line shape of $D_{s1}(2536) \rightarrow D^{*0}K$ one can determine $\Gamma_{\pi^0\gamma}$ without reconstructing neither neutral pions nor photons. This measurement shows good statistical accuracy ($\Gamma_{\pi^0\gamma}$=1.57±0.06) and is compatible to the BaBar results ($\Gamma_{\pi^0\gamma}$=1.74±0.02±0.13)[5] if systematic uncertainties would have been included.

In a second study of $D_{s1}(2536) \rightarrow D^{*0}K$ the ratio of helicity amplitudes squared $R_\Lambda = |A_{10}|^2 / |A_{00}|^2$ was measured to be $R_\Lambda = 2.65 \pm 0.24$. This value is consistent with the Belle measurement of $R_\Lambda = 3.6\pm0.3\pm0.1$[4] if further systematic uncertainties would have been considered. To compare the data presented in this thesis to the Belle measurement of $\Gamma_D/\Gamma_{tot} = 0.38 \pm 0.05 \pm 0.01$ four extreme scenarios were studied: pure S-wave ($\Gamma_D/\Gamma_{tot} = 0$), pure D-wave ($\Gamma_D/\Gamma_{tot} = 1$), $|A_{10}|^2 = 1$ ($\Gamma_D/\Gamma_{tot} = 1/3$) and $|A_{00}|^2 = 1$ ($\Gamma_D/\Gamma_{tot} = 2/3$). For these cases no measurement of the phase ϕ_{10} is necessary to calculate Γ_D/Γ_{tot}. The HQET hypothesis of a pure D-wave decay gives the second worst fit result: $\chi^2/ndf \approx 11$ and is not consistent with the data presented in this thesis. Only the fit with $|A_{00}| = 1$ shows a worse result:
$\chi^2/ndf \approx 29$. In the other cases (pure S-wave and $|A_{10}|^2 = 1$) relative accurate fit results were obtained ($\chi^2/ndf \approx 2.5$ and $\chi^2/ndf \approx 2$) respectively. The Belle results of $\Gamma_D/\Gamma_{tot} = 0.38\pm0.05\pm0.01$ ($R_\Lambda = 3.6$) describes the data quite well: $\chi^2/ndf \approx 1.1$.

Another objective of this thesis is the search for new D_{sJ} states. Since more sophis-

ticated models based on HQET, especially the model of Close [15], predict numerous new D_{sJ} states, their search is of major interest. CDF can contribute to this search by confirming the existence of the $D_{sJ}(2860)$, seen by BaBar [1], and $D_{sJ}(2700)$, detected by BaBar and Belle [1, 2] states.

In addition $D_{s2}(2573)$ is seen in the decay mode $D_{s2}(2573) \to D^{*0}K$. It is the first observation of $D_{s2}(2573)$ in this decay mode.

Further steps in the near future are the analysis of systematic uncertainties for all results as well as the measurement of the production ratio of $D_{s1}(2536)/D_{s2}(2573)$ and the branching ratio $D_{s2}(2573) \to D^{*0}K/D_{s2}(2573) \to D^{0}K$.

A Appendix

A.1 List of Variables tested for mass dependence

Correlation after cuts	Correlation before cuts	Removed	Name
12.0974382 %	33.4083236 %	x	DsSK_Pt
10.1421771 %	12.2944082 %	x	D_Pt
7.90235407 %	9.25640793 %	x	DPi_Pt
7.12076751 %	6.32036388 %	x	DPi_PtSigni
7.02227509 %	21.1885378 %	x	DsSK_PtSigni
5.75540884 %	8.769239 %	x	DK_Pt
4.71615468 %	5.68948543 %	x	DK_PtSigni
4.55522005 %	11.2494305 %	x	DsSK_Eta
4.13633018 %	10.6259952 %	x	DsSK_D0
4.11556624 %	5.63598859 %	x	DsSK_MatchedSvt
4.04963406 %	4.77523162 %	x	D_D0
3.95422048 %	4.55236421 %	x	D_D0Signi
3.82530885 %	11.0577723 %	x	TriggerFlag
3.1841122 %	2.74501593 %	x	D_Eta
3.10260139 %	8.89838777 %	x	DsSK_NSiAxHits
2.99865759 %	20.5831234 %	x	DsSKPID_pullTofKa
2.98764435 %	2.38499907 %	x	DK_Eta
2.8799231 %	8.03582506 %	x	PseudoTriggerFlag
2.8715161 %	4.07861444 %	x	D_Lxy
2.79825921 %	3.64727918 %		Isolation_Iso
2.59419361 %	2.38637432 %	x	DPi_Eta
2.49743727 %	9.47601179 %		DsSK_NSiStHits
2.37935574 %	6.68298462 %	x	DsSK_D0Signi
2.29998103 %	1.62162396 %		DPi_NCotStHits
2.15416054 %	2.02277889 %		DK_NCotStHits
1.80029809 %	14.9013321 %		DsSKPID_DeDx
1.79018456 %	4.02506318 %		D_ct
1.75729876 %	2.52504398 %		DKPID_ratioKaon
1.72855859 %	1.88964874 %		D_Mass
1.68922432 %	1.63322501 %		DPi_NCotAxHits
1.58564187 %	1.86098856 %		DK_NCotAxHits
1.56857396 %	2.94068129 %		D_LxySigni

Correlation after cuts	Correlation before cuts	Removed	Name
1.54669994 %	12.8410341 %		DsSK_NCotStHits
1.50377026 %	18.7163716 %		DsSKPID_ratioKaon
1.1087193 %	0.893241129 %		DPiPID_ratioPion
1.05412152 %	2.07674661 %		D_Chi23D
1.0455691 %	16.0105193 %		DsSK_NCotAxHits
1.01829109 %	0.516225775 %		DPi_NSiStHits
0.986963689 %	2.07709494 %		D_Prob
0.626063466 %	0.530032897 %		DPi_NSiAxHits
0.56999296 %	0.59940402 %		DK_NSiStHits
0.527118912 %	0.724665434 %		DK_NSiAxHits
0.477676454 %	1.0671588 %	x	DK_D0Signi
0.455029008 %	1.01178785 %	x	DPi_D0Signi
0.433844589 %	1.41375981 %	x	DPi_D0
0.181915306 %	1.9938936 %	x	DK_D0

Table A.2: Correlation to the Q-value before and after applying further selection requirements.

A.2 List of Variables used for Training

Variable name	additional significance	significance only this variable	significance loss when removed	global correlation to others	PrePro Flag
DsSKPID_ratioKaon	204.40	204.40	113.00	64.9%	14
Isolation_Iso	159.97	170.69	121.23	35.8%	34
DKPID_ratioKaon	91.89	131.18	56.61	35.1%	34
D_Mass	70.37	114.42	57.46	31.8%	14
DPiPID_ratioPion	58.07	85.78	56.97	25.0%	34
DsSK_NSiStHits	56.56	68.88	53.84	20.0%	19
DsSKPID_DeDx	48.07	178.86	46.17	65.9%	34
D_LxySigni	35.62	62.44	32.88	60.2%	14
DPi_NCotStHits	20.83	83.47	19.48	42.9%	14
DK_NCotAxHits	20.67	26.43	22.24	38.9%	14
D_Prob	13.75	41.51	6.47	99.7%	34
DPi_NCotAxHits	10.78	76.95	10.34	40.5%	14
D_ct	7.98	46.36	8.02	60.6%	14
DK_NSiAxHits	7.79	25.29	7.74	40.9%	14
D_Chi23D	5.39	41.12	5.39	99.7%	14
DsSK_NCotStHits	4.45	24.39	5.58	34.3%	14
DK_NCotStHits	4.95	37.81	4.73	40.6%	14
DsSK_NCotAxHits	4.39	30.55	4.39	26.8%	14
DK_NSiStHits	1.85	18.59	1.87	40.1%	19
DPi_NSiAxHits	0.33	20.29	0.24	42.8%	14
DPi_NSiStHits	0.17	18.63	0.17	42.2%	19

Table A.3: List of Variables used for network training to select $D_{s1}(2536)$ and $D_{s2}(2573)$.

A.3 Signal Purity Distributions for all training variables

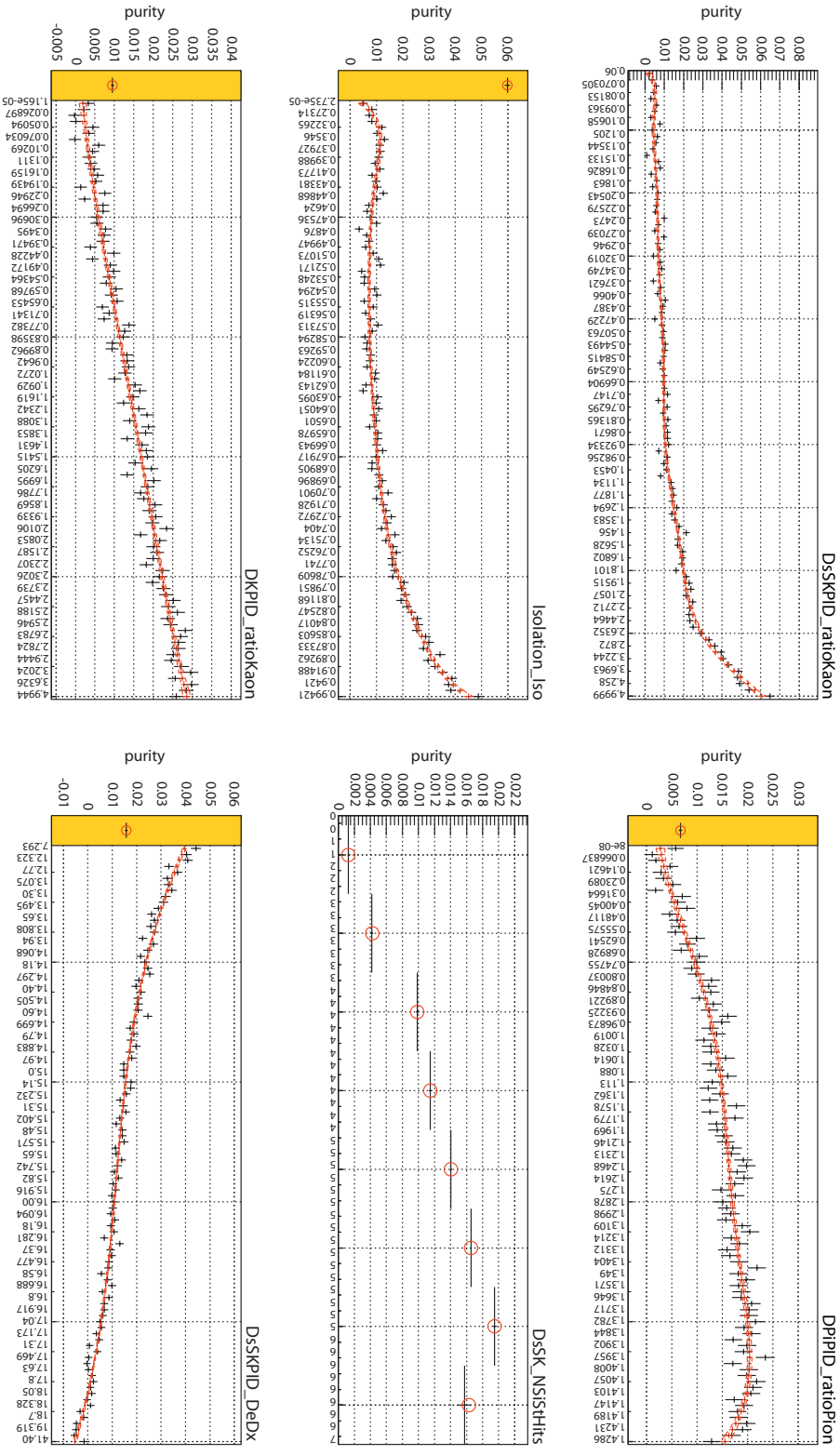

Figure A.1: Purity plots of Variables used for network training to select $D_{s1}(2536)$ and $D_{s2}(2573)$.

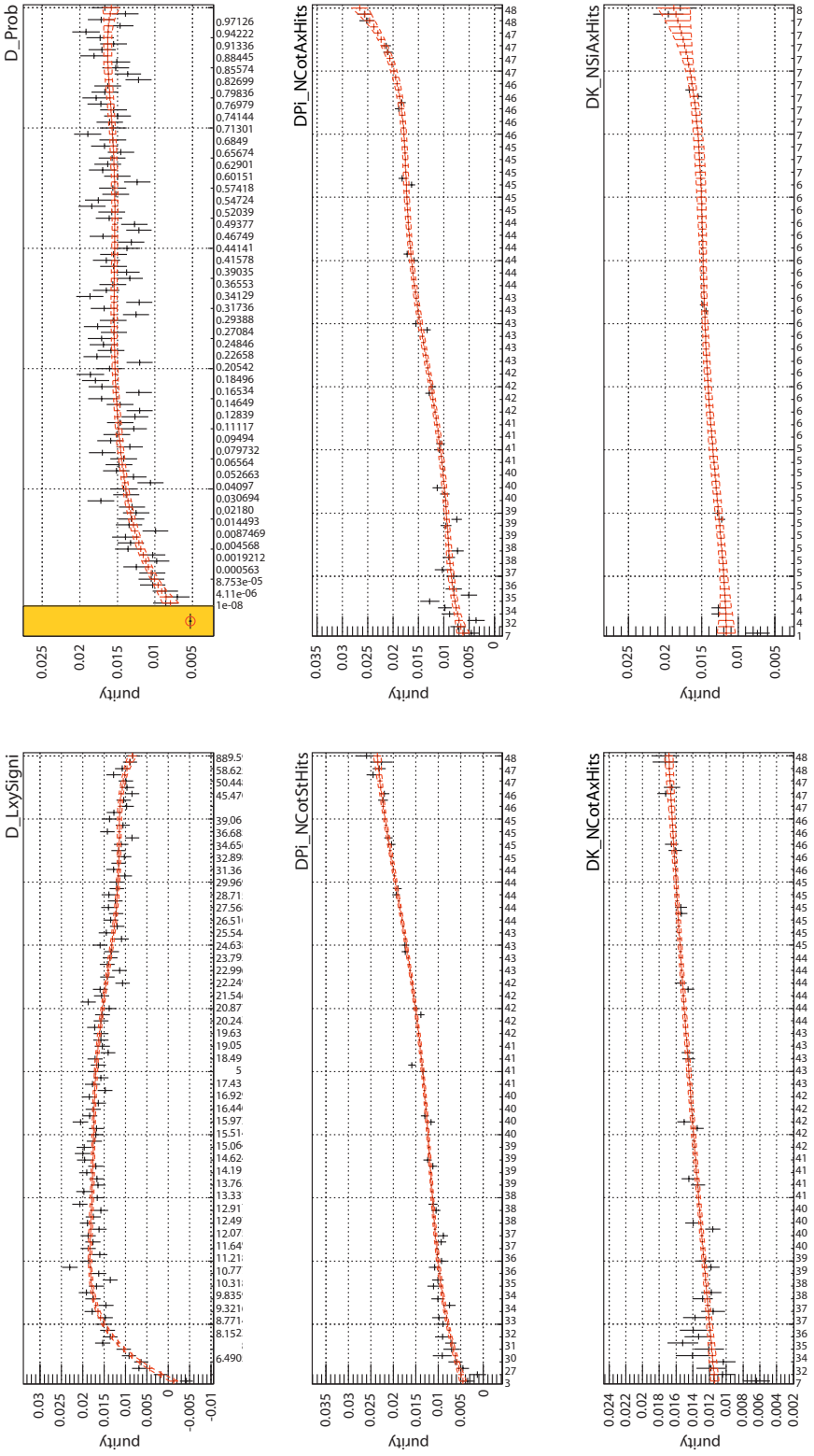

Figure A.2: Purity plots of Variables used for network training to select $D_{s1}(2536)$ and $D_{s2}(2573)$.

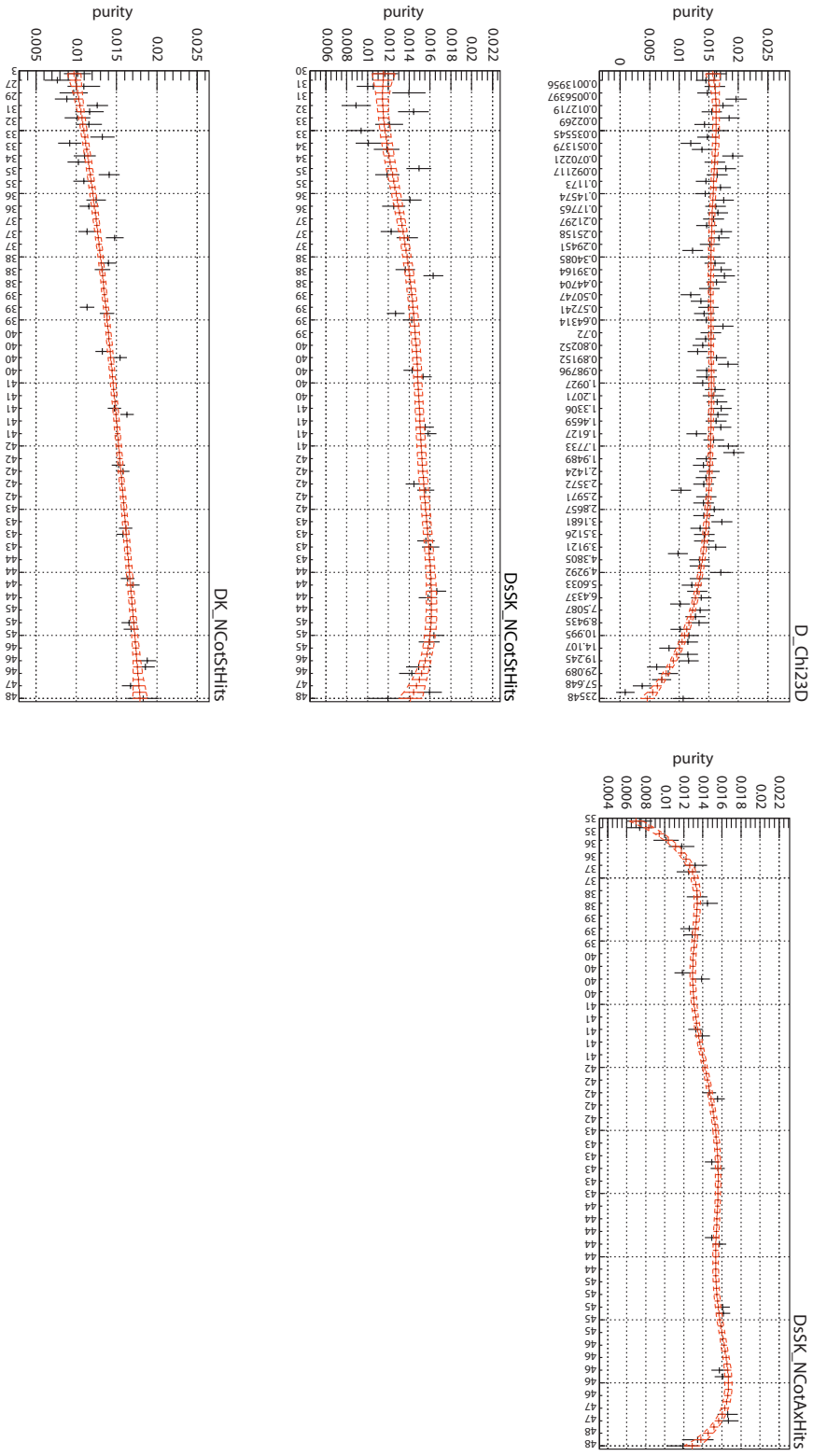

Figure A.3: Purity plots of Variables used for network training to select $D_{s1}(2536)$ and $D_{s2}(2573)$.

A.4 Angles after Phase Space Monte Carlo

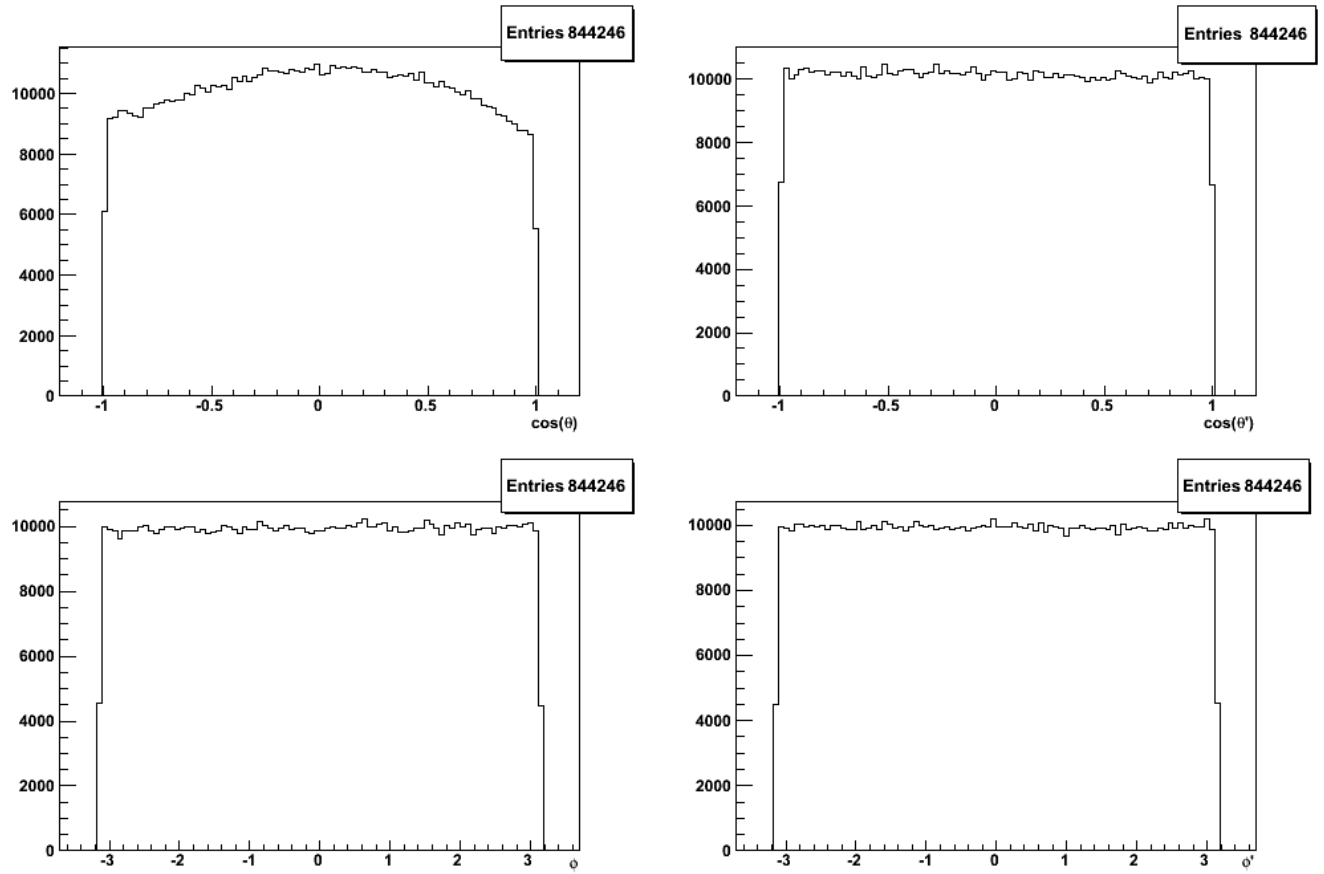

Figure A.4: Angles after phase space Monte Carlo

Bibliography

[1] B. Aubert et al. [BABAR Collaboration]. Observation of a new D/s meson decaying to D K at a mass of $2.86 - GeV/c^2$. *Phys. Rev. Lett.*, 97:222001, 2006,].

[2] J. Brodzicka et al. [Belle Collaboration]. Observation of a new D_{sJ} meson in $B^+ - > D_0 B D_0 K^+$ decays. *Phys. Rev. Lett.*, 100:092001, 2008, arXiv:0707.3491 [hep-ex].

[3] C. Amsler et al. [Particle Data Group Collaboration]. Review of particle physics. *Phys. Lett.*, B667:1, 2008.

[4] Belle Collaboration. Observation of $D_{s1}(2536)$ -> $D^+\pi^-K^+$ and angular decomposition of $D_{s1}^+(2536) - > D^{**+}K_0^S$, 2007.

[5] B. Aubert et al. [BABAR Collaboration]. Measurement of the branching ratios $\Gamma(D_s^{*+} \to D_s^+\pi^0)/\Gamma(D_s^{*+} \to D_s^+\gamma)$ and $\Gamma(D^{*0} \to D^0\pi^0)/\Gamma(D^{*0} \to D^0\gamma)$. *Phys. Rev.*, D72:091101, 2005,].

[6] B. Aubert et al. [BABAR Collaboration]. A study of the $D_{sJ}(2317)$ and $D_{sJ}(2460)$ mesons in inclusive c anti-c production near $s^{1/2} = 10.6$-GeV. *Phys. Rev.*, D74:032007, 2006,].

[7] James P. Alexander et al. [CLEO Collaboration]. Production and decay of the $D_{s1}(2536)$. *Phys. Lett.*, B303:377–384, 1993.

[8] Stephen Godfrey and Richard Kokoski. The Properties of p Wave Mesons with One Heavy Quark. *Phys. Rev.*, D43:1679–1687, 1991.

[9] J. Zeng, J. W. Van Orden, and W. Roberts. Heavy mesons in a relativistic model. *Phys. Rev.*, D52:5229–5241, 1995,].

[10] Suraj N. Gupta and James M. Johnson. Quantum chromodynamic potential model for light heavy quarkonia and the heavy quark effective theory. *Phys. Rev.*, D51:168–175, 1995,].

[11] D. Ebert, V. O. Galkin, and R. N. Faustov. Mass spectrum of orbitally and radially excited heavy- light mesons in the relativistic quark model. *Phys. Rev.*, D57:5663–5669, 1998,].

[12] T. A. Lahde, C. J. Nyfalt, and D. O. Riska. Spectra and M1 decay widths of heavy-light mesons. *Nucl. Phys.*, A674:141–167, 2000,].

[13] Massimo Di Pierro and Estia Eichten. Excited heavy-light systems and hadronic transitions. *Phys. Rev.*, D64:114004, 2001,].

[14] Takayuki Matsuki and Toshiyuki Morii. Spectroscopy of heavy mesons expanded in 1/m(Q). *Phys. Rev.*, D56:5646–5667, 1997,].

[15] F. E. Close, C. E. Thomas, Olga Lakhina, and E. S. Swanson. Canonical Interpretation of the $D_{sJ}(2860)$ and $D_{sJ}(2690)$. *Physics Letters B*, 647:159, 2007.

[16] T. Barnes, F. E. Close, and H. J. Lipkin. Implications of a dk molecule at 2.32 gev. *Physical Review D*, 68:054006, 2003.

[17] Hai-Yang Cheng and Wei-Shu Hou. B decays as spectroscope for charmed four-quark states. *Physics Letters B*, 566:193, 2003.

[18] M. Nielsen, R. D. Matheus, F. S. Navarra, M. E. Bracco, and A. Lozea. Diquark-antidiquark with open charm in qcd sum rules, 2005.

[19] K. Terasaki. Babar resonance as a new window of hadron physics. *Physical Review D*, 68:011501, 2003.

[20] Dae Sung Hwang and Do-Won Kim. Decay Constants of $D^*_{sJ}(2317)$ and $D_{sJ}(2460)$. *Physics Letters B*, 606:116, 2005.

[21] Eef van Beveren and George Rupp. Observed $D_s(2317)$ and tentative D(2100-2300) as the charmed cousins of the light scalar nonet. *Physical Review Letters*, 91:012003, 2003.

[22] Dae Sung Hwang and Do-Won Kim. Mass of $D_{sJ}(2317)$ and coupled channel effect. *Phys. Lett.*, B601:137–143, 2004,].

[23] Eric S. Swanson. The new heavy mesons: A status report. *Phys. Rept.*, 429:243–305, 2006,].

[24] M. Feindt and U. Kerzel. The NeuroBayes neural network package. *Nucl. Instrum. Meth.*, A559:190–194, 2006.

[25] Muriel Pivk and Francois R. Le Diberder. splot: a statistical tool to unfold data distributions. *NUCL.INSTRUM.METH.A*, 555:356, 2005.

[26] Christopher S. Hill [On behalf of the CDF Collaboration]. Operational experience and performance of the CDFII silicon detector. *Nucl. Instrum. Meth.*, A530:1–6, 2004.

[27] A. Sill [CDF Collaboration]. CDF Run II silicon tracking projects. *Nucl. Instrum. Meth.*, A447:1–8, 2000.

[28] Anthony A. Affolder et al. [CDF Collaboration]. Intermediate silicon layers detector for the CDF experiment. *Nucl. Instrum. Meth.*, A453:84–88, 2000.

[29] Anthony Allen Affolder et al. [CDF Collaboration]. CDF central outer tracker. *Nucl. Instrum. Meth.*, A526:249–299, 2004.

[30] D. Acosta et al. [CDF-II Collaboration]. A time-of-flight detector in CDF-II. *Nucl. Instrum. Meth.*, A518:605–608, 2004.

[31] A. Artikov et al. Design and construction of new central and forward muon counters for CDF II. *Nucl. Instrum. Meth.*, A538:358–371, 2005,].

[32] Robert Downing et al. Track extrapolation and distribution for the CDF-II trigger system. *Nucl. Instrum. Meth.*, A570:36–50, 2007,].

[33] B. Aubert et al. [BABAR Collaboration]. Observation of a narrow meson decaying to $D_s^+\pi^0$ at a mass of 2.32-GeV/c^2. *Phys. Rev. Lett.*, 90:242001, 2003,].